Diurnal Variations of Low-Level Winds and Precipitation Response to Large-Scale Circulations during a Heavy Rainfall Event

WENXIN ZENG, GUIXING CHEN, AND YU DU

School of Atmospheric Sciences, and Guangdong Province Key Laboratory for Climate Change and Natural Disaster Studies, Sun Yat-sen University, Guangzhou, and Southern Marine Science and Engineering Guangdong Laboratory (Zhuhai), Zhuhai, China

ZHIPING WEN

Department of Atmospheric and Oceanic Sciences, and Institute of Atmospheric Sciences, Fudan University, Shanghai, China

(Manuscript received 1 May 2019, in final form 16 August 2019)

ABSTRACT

A succession of MCSs developed during the last week of October 2016 and produced extreme heavy rainfall in central China. The event underwent an evident shift from a mei-yu-like warm scenario to an autumn cold scenario. Diurnal cycles of rainfall and low-level winds may be modulated by the shifting of large-scale atmospheric conditions. We conducted observational analyses and numerical experiments to examine how large-scale circulations influenced rainfall systems through diurnally varying processes. The results show that, in the first half (warm) period of the event, intense rainfall mostly occurred in eastern-central China with an early morning peak. It was closely related to a nocturnal southwesterly low-level jet (NLLJ) on the flank of the western Pacific subtropical high. The NLLJ formed near midnight in southern China where ageostrophic wind rotated clockwise due to Blackadar's inertial oscillation. The NLLJ extended downstream to central China during the predawn hours due to the horizontal advection of momentum. Both the formation and extension of the NLLJ were supported by an enhanced subtropical high that provided relatively warm conditions with surface heating for boundary layer inertial oscillation and strong background southwesterly winds for momentum transport. The NLLJ induced MCSs at its northern terminus where the low-level ascent, moisture flux convergence, and convective instability were enhanced during the predawn hours. In the second half period with an intrusion of cold air, the diurnal amplitude of low-level winds became small under relatively cold and cloudy conditions. Moderate rainfall tended to occur in western-central China with a peak after midnight, most likely due to frontogenetic processes, upslope lifting, and nighttime cloud-top cooling.

1. Introduction

Diurnal variations of low-level winds and rainfall are important aspects of climate and weather over East Asia (Ohsawa et al. 2001; Wang et al. 2004; Johnson 2006; Monaghan et al. 2010; Yuan et al. 2013; Du et al. 2014; Yu et al. 2014). The observed diurnal amplitude is large during warm season and becomes relatively small during cold season (Li et al. 2008b; Yin et al. 2009; Chen et al. 2009b, 2013; Yuan et al. 2010). Such evident seasonality of diurnal cycles may express a regional response to the seasonal changes in solar heating and general circulations. Further studies of the diurnally varying processes in winds and precipitation systems are important to improve our understanding of regional climate (Yang and Smith 2006) and extreme weather (Trier et al. 2014).

The diurnal variations of low-level winds have been recognized as a regional key feature driven by thermodynamic/dynamic forcings in the boundary layer and effects of topography. The wind maxima tend to appear at night and sometimes form a nocturnal low-level jet (NLLJ) particularly over the plains (Rife et al. 2010; Du et al. 2014). The wind diurnal variations may be attributed to a clockwise rotation of the ageostrophic wind as indicated by Blackadar's inertial oscillation in the boundary layer (Blackadar 1957; Du and Rotunno 2014; Shapiro et al. 2016). The wind diurnal variations may also be driven by the diurnally varying pressure gradient force due to differential heating/cooling on sloped terrains (Holton 1967; Parish and Oolman 2010; Fedorovich et al. 2017). As a result, the wind diurnal variations are

Corresponding author: Guixing Chen, chenguixing@mail.sysu.edu.cn

DOI: 10.1175/MWR-D-19-0131.1

observed to exhibit an evident regionality with complex topography over East Asia and North America.

The diurnal variations of winds and precipitation also vary seasonally over East Asia, as the regional forcings may be regulated by different atmospheric conditions. During the warm season, the low-level winds tend to strengthen at night and their diurnal amplitude is particularly large over southeastern China where the southwesterly monsoon is prevalent (Chen et al. 2009b, 2013; Xue et al. 2018). The induced rainfall usually maximizes overnight in the eastern slopes of the Tibetan Plateau and in the morning over the eastern China plains (Yu et al. 2007; Geng and Yamada 2007; Chen et al. 2009a; Yin et al. 2009; Yuan et al. 2012; Wu et al. 2018). The morning rainfall is sometimes intense, as the nocturnal MCSs may develop successively under anomalous large-scale circulations coupled with repeated wind diurnal variations in several days (Carbone and Tuttle 2008; Wang et al. 2014; Trier et al. 2017). For instance, Chen et al. (2017) revealed that the strong NLLJ in the monsoon flow may impinge on the mei-yu front and trigger several MCSs at night, producing heavy rainfall in a narrow latitudinal band. Xue et al. (2018) noted that the accelerated ageostrophic wind in the southwesterly monsoon can strengthen net moisture flux and provide preconditions for the morning peak in mei-yu rainfall.

During the cold season, the diurnal cycle of low-level winds becomes weak, and the rainfall mostly occurs in the eastern slopes of the Tibetan Plateau with a maximum after midnight (e.g., Li et al. 2008b; Chen et al. 2009a; Li and Yu 2014). This nocturnal rainfall may be attributed to local mountain–plains solenoid and orographic lifting in the foothills (Bao et al. 2011; Zhang et al. 2018). The nocturnal rainfall is also influenced by the cloud-top radiative cooling that may increase relative humidity at night in the context of the prevalent clouds during the cold season (Li and Yu 2014; Huang and Chang 2018). The seasonal difference in diurnal cycles suggests a strong response to regional forcings and large-scale atmospheric conditions (e.g., southwesterly monsoon, subtropical high, and midlatitude fronts) (Trier et al. 2006; Wang et al. 2012; Rao et al. 2019). Therefore, further studies on the transition of synoptic conditions from warm to cold scenarios and consequently induced diurnal cycles may improve our understanding of multiscale processes in heavy rainfall events.

Some studies have examined the regulation of large-scale circulation on the locations and timing of MCSs through diurnal processes over North America (e.g., Augustine and Caracena 1994; Tuttle and Davis 2006; Trier et al. 2017) and East Asia (Chen et al. 2017; Xue et al. 2018; Zhang et al. 2018). Most of these studies focused on a given large-scale condition particularly in a warm-season scenario. We may expect that the locations and timing of rainfall systems change with different atmospheric conditions, which can interact constructively with regional diurnal variations. Trier et al. (2014) conducted sensitivity numerical simulations and stated that convection systems respond strongly to the changes in synoptic-scale patterns that influence the LLJ and surface front. To date, there is still a lack of comprehensive studies evaluating the diurnal cycle of rainfall systems in the context of realistic shifting large-scale conditions over East Asia.

The overall motivation of this study is to clarify how the diurnal cycle of successive rainfall systems responds to the large-scale circulation that itself undergoes evident transition from warm to cold conditions. To address this key question, we examine the connection of rainfall systems to wind diurnal variations and how this connection changes as the synoptic conditions change. We chose to study a long-duration heavy rainfall period when the synoptic conditions shifted from a mei-yu-like warm-season scenario to an autumn cold-season scenario. The rest of this study is organized as follows. In section 2, the datasets and the setup of numerical experiments are described. In section 3, the diurnal variations of low-level winds and rainfall systems as well as their relationships with the changing atmospheric conditions are presented. The mechanisms governing wind diurnal variations and the role of large-scale conditions are elucidated in section 4. In section 5, the detailed impact of wind diurnal variations on the development of MCSs is demonstrated. Finally, the conclusion and discussion are given in section 6.

2. Data and methods

a. Rainfall and reanalysis data used in this study

In this study, we focus on a long-duration heavy rainfall event from 24 October to 31 October 2016. To show the observed rainfall systems, we use the satellite data of NOAA Climate Prediction Center morphing technique (CMORPH). The CMORPH data offers a rain rate at fine temporal intervals of 30 min and a horizontal resolution of 8 km (Joyce et al. 2004). This high-resolution dataset can be used to examine the details of rainfall systems such as their diurnal cycles (e.g., Janowiak et al. 2005). The CMORPH data have been applied to resolve the rainfall diurnal cycles over East Asia, although it somewhat underestimates the climatology of morning-peak rainfall (Shen et al. 2010; Luo et al. 2013). Chen et al. (2016) found that the CMORPH data are consistent with the rain gauge observations in revealing regional rainfall events with mesoscale details. It also well captures the patterns of rainfall diurnal cycles

over complex terrain and the seasonal/intraseasonal variations in rainfall diurnal cycle over southern China (Chen et al. 2018; Chen et al. 2019). As the CMORPH data may represent the rainfall response to terrain and changes in atmospheric conditions, it will be used for the observational analysis of this study.

To show atmospheric conditions and their diurnal cycles, we use the global reanalysis dataset of the 55-yr Japanese Reanalysis Project (JRA-55) (Kobayashi et al. 2015). JRA-55 provides assimilated atmospheric variables at a horizontal resolution of 1.25° and temporal intervals of 6 h (0000, 0600, 1200, and 1800 UTC). The dataset has 37 vertical pressure levels with intervals of 25 hPa below 700 hPa, offering a good representation of atmospheric conditions in the lower troposphere where the diurnal variability in winds and temperature is large. Chen et al. (2014) assessed four mainstream reanalysis datasets and found that JRA-55 had the best verification scores in representing the diurnal variability over East Asia. In the numerical simulation for further investigation on MCSs and their response to large-scale conditions, we use the Final Global Data Assimilation System (FNL) reanalysis data. The FNL dataset has relatively fine resolution of 1° horizontal grids and 6-hourly time steps. The FNL has been widely used as initial and lateral boundary conditions to drive numerical models in previous studies that analyzed the diurnal variations over East Asia (e.g., Liu et al. 2012; Du et al. 2014).

b. *Setup of the numerical experiments*

A numerical simulation is conducted using the Advanced Research Weather Research and Forecasting (WRF) Model (Skamarock and Klemp 2008). The WRF Model has been used to simulate the diurnal variations that are usually active in nocturnal environments over China (e.g., Du et al. 2014; Xue et al. 2018). To reproduce the rainfall event, the WRF simulation is initiated at 2000 LT 23 October (local time, LT = UTC + 8 h) and ran for 180 h until 0800 LT 1 November. Because we focus on the regional diurnal variations and mesoscale rainfall systems under shifting large-scale conditions over an 8-day period, a large model domain with reasonable fine mesh is needed. A compromise is made that a horizontal resolution of 9 km is applied to a domain of 300 × 300 grids and 50 vertical layers in terrain-following coordinates. A similar setup of a 9-km-spacing experiment was applied to reasonably depict synoptic-scale mei-yu front and monsoon flow, together with embedded mesoscale disturbances and diurnal variations during another heavy rainfall event in this region (Chen et al. 2017). Previous studies noted that the models at higher resolutions may perform better in simulating rainfall intensity (Li et al. 2008a; Dirmeyer et al. 2012; He et al. 2015; Zhu et al. 2018). However, the spatial pattern and diurnal phase of rainfall are somewhat insensitive to model resolutions (Sun and Zhang 2012; Du et al. 2014), which should be our focus rather than the rainfall intensity.

In the WRF simulation, we adopt parameterization schemes such as the Kain–Fritsch convective scheme, the Yonsei University (YSU) boundary layer scheme, the new Thompson microphysics scheme, the RRTMG longwave and shortwave radiation schemes and the Noah land surface scheme. The Kain–Fritsch scheme has been shown to perform well in capturing the diurnal phase of the mei-yu rainfall in China, although it may overestimate rainfall intensity at 9-km grid spacing (Cai et al. 2018; Zheng et al. 2016). As the YSU scheme may struggle in nocturnal environments in old versions of the WRF (Hu et al. 2013), we used the recent version 3.8.1 to reduce the uncertainty. The new Thompson scheme is good at reproducing moderate to heavy rainfall over southeastern China (Li and Tang 2012), although it has some difficulty in developing realistic cold pools at night over the United States (Johnson et al. 2018). An overall evaluation of Zhu et al. (2018) stated that the WRF Model reproduces well the rainfall diurnal cycles over East Asia, especially in terms of spatial patterns and peak hours. In section 3, we also see that the WRF Model performs reasonably in simulating the selected event of this study despite of some bias in rainfall intensity and location. Since the uncertainty in the mesoscale model and the quantitative evaluation of model performance are beyond the scope of this study, we will examine the spatial patterns and diurnal phases of simulated rainfall in a qualitative manner.

3. Characteristics of heavy rainfall and associated atmospheric conditions

a. *Spatial pattern and diurnal variations of precipitation*

Figure 1a shows that the accumulative rainfall over the last 8 days in October 2016 mainly occurred in 26°–34°N. The CMORPH data showed a maximum of the 8-day total accumulated rainfall exceeding 200 mm in eastern-central China (28.5°–31°N, 113.5°–122°E) and a secondary maximum of ~100 mm in western-central China (26°–28.5°N, 105°–113.5°E). During the first half period of the event (24–27 October), strong rainfall occurred mostly in eastern-central China, which was analogous to the climatological pattern of summer rainfall (Ding and Chan 2005). During the second half period (28–31 October), moderate rainfall occurred in western-central China, which resembled the typical pattern in autumn (Ding and Wang 2008). The rainfall amount in late October 2016 increased by ~200% (~50%) in

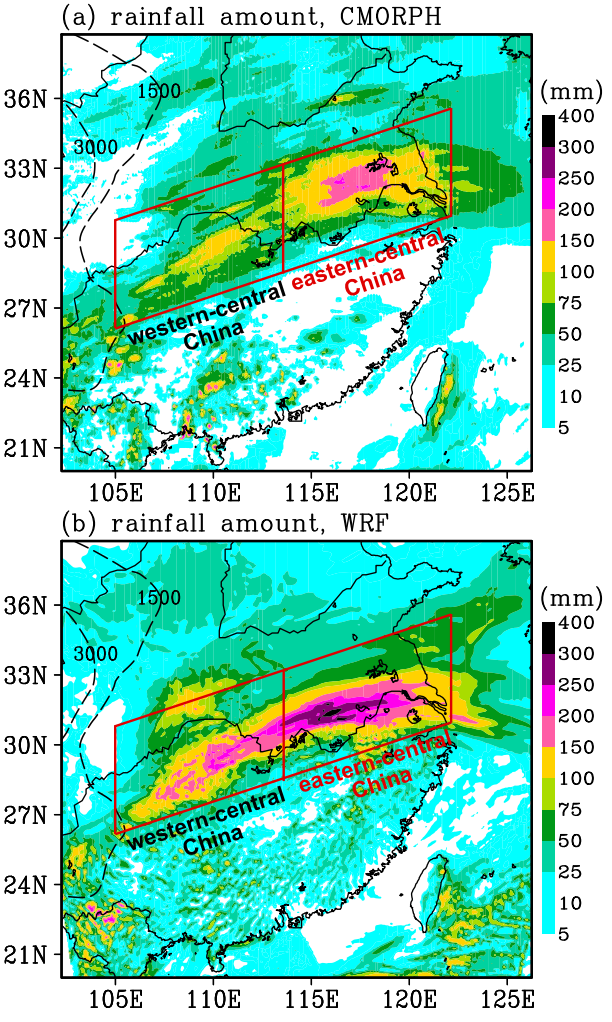

FIG. 1. Accumulated rainfall amount (mm) during 24–31 Oct 2016, derived from (a) the CMORPH dataset and (b) the WRF result. The large red parallelogram denotes the rainband in central China (105°–122°E) with left domain denotes eastern-central China (105°–113.5°E) and right one denotes western-central China (113.5°–122°E).

eastern-central (western-central) China, compared to the climate mean (not shown). Such a long-duration event produced extremely anomalous rainfall (monthly report of CMA https://cmdp.ncc-cma.net/Monitoring/en_moni_info.php?catId=2), whose extended duration and severity have been underestimated in operational forecasts. Figure 1b shows that the WRF simulation reasonably reproduces the southwest–northeast-oriented rainband in central China. The WRF reproduces the spatial patterns of the rainfall that is stronger in eastern-central China than in western-central China. It also reproduces the scattered rainfall in southern China and the widespread rainfall in northern China, which are consistent with the CMORPH data. We note that the WRF Model overestimates the two regional maxima of rainfall amount over central China (note that the shading scale is nonlinear), possibly due to the adoption of convective parameterization at 9-km grid spacing (Zheng et al. 2016). However, we focus more on the patterns and diurnal phases of rainfall during the event, which are reasonably captured by our WRF simulation.

To show the detailed evolution of rainfall systems, we examine the longitude–time variations of the satellite-observed rain rate along the orientation of the rainband. Figure 2a shows that the rainfall gradually developed from the eastern slopes of the Yun-gui Plateau to eastern-central China during the first half period. In particular, two rainfall systems grew at 113°E and propagated eastward during the predawn on 26–27 October. The mean rain rate above 1 mm h^{-1} had a horizontal scale of 200–400 km, indicating the rain produced by MCSs as marked by "A" and "B." The MCSs produced rainfall of more than 50 mm day^{-1} in eastern-central China. Such successive MCSs are analogous to the rainfall systems observed in the mei-yu season (Sun and Zhang 2012; Chen et al. 2017; Zhang et al. 2018). After 28 October, two rainfall systems mainly occurred at 105°–110°E in western-central China, as marked by "C" and "D." The rainfall became relatively moderate but widespread, which is similar to that of the prevalent stratiform rainfall during the cold season (Li et al. 2008b). The differences in rainfall systems during the two periods indicate a seasonal transition from warm to cold conditions. Figure 2b shows that the WRF reproduces the two MCSs that propagated eastward in eastern-central China on 26–27 October. It also reproduces the relatively moderate rainfall after 28 October and the location of rainfall systems shifted to eastern-central China.

Figure 2c shows that the observed rainfall in eastern-central China had a maximum rate exceeding 2 mm h^{-1} on 26–27 October. The rainfall increased since midnight (~2300 LT), reached its peak in the morning (~0800 LT), and dissipated around noon. The WRF Model reproduces the intense morning rainfall on 26 October, while it gives an earlier peak on 27 October than the observations. The WRF Model also reproduces the transition to relatively moderate rainfall on 28 October. Figure 2d shows that in western-central China, the observed rainfall increased on 28–29 October. The rainfall is usually intensified after midnight and maximized during the predawn hours (0200–0500 LT). The WRF Model reproduces the enhanced nighttime rainfall on 28–29 October. However, it overestimates the rainfall intensity possibly due to the relatively coarse resolution and the Kain–Fritsch convective scheme, and the overestimation of rainfall may be reduced in convective-permitting simulation (e.g., Zhu et al. 2018). Nevertheless, the WRF

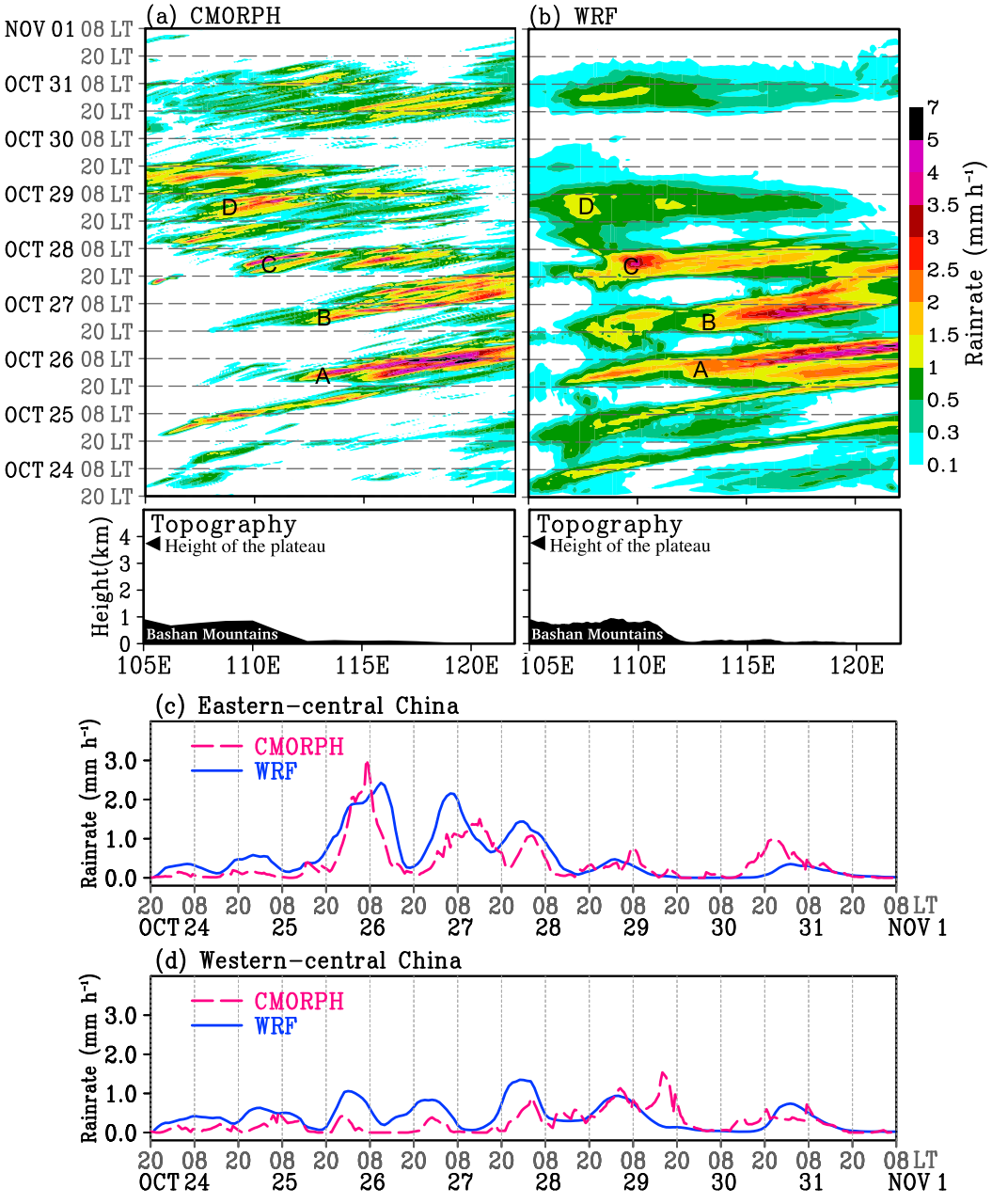

FIG. 2. Longitude–time variations of rain rate (mm h^{-1}) in central China (along the red parallelogram in Fig. 1) during 24–31 Oct 2016, derived from (a) the CMORPH estimation and (b) the WRF result. The rainfall systems are denoted by "A"–"D." The averaged topography (km) is plotted below. Mean rain rate (mm h^{-1}) over (c) eastern-central China and (d) western-central China.

Model reasonably represents the spatial patterns of rainfall diurnal variations and their shifts from a relatively warm scenario to a cold scenario.

b. Large-scale atmospheric conditions and associated wind diurnal variations

In this section, we examine the daily evolution of large-scale atmospheric conditions and related wind diurnal variations. Figure 3a shows that in the first period, the western Pacific subtropical high (WPSH) extended to southeastern China. It strengthened from 25 to 27 October, with an anomaly of 500-hPa geopotential height up to ~100 gpm (Fig. 3c). Along with the enhanced WPSH, southeastern China was characterized by high pressure and a temperature greater than 288 K in the lower troposphere (Figs. 3a,d). In central China near

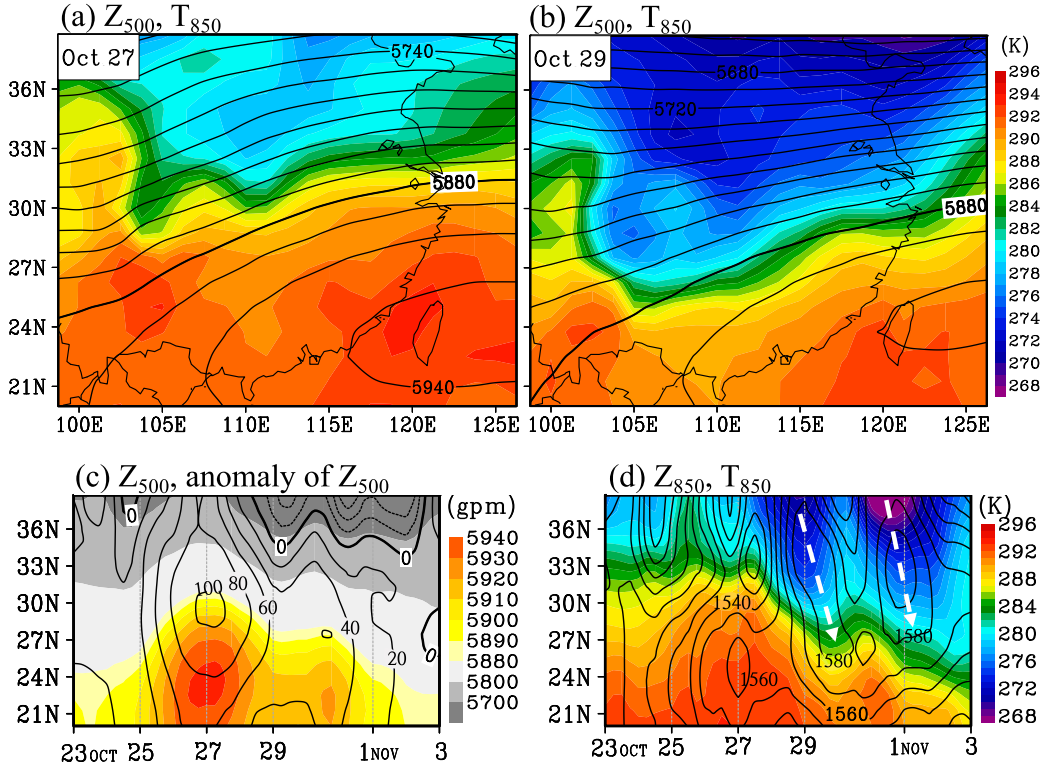

FIG. 3. Daily mean of 500-hPa geopotential height (gpm, contours) and 850-hPa temperature (K, shading) on (a) 27 Oct and (b) 29 Oct. Time–latitude diagram at 117.5°E of (c) 500-hPa geopotential height (gpm, shading) and its anomaly (gpm, contours), and (d) 850-hPa temperature (K, shading) and geopotential height (gpm, contours). All these plots are derived from the JRA-55 reanalysis data. The dashed arrows in (d) show the intrusions of cold air with high pressure.

30°–33°N, there was a large temperature gradient, indicating a frontal zone to the north of the WPSH. Such synoptic patterns resemble the mei-yu-like warm-season scenario, which is favorable for convection development in the zonally oriented rainband over East Asia (Ninomiya 2000; Ding and Chan 2005).

Figures 3b and 3c show that after 28 October, the WPSH weakened slightly with an anomaly of ~40 gpm at 500 hPa over southern China. However, in the lower troposphere, there was high pressure with cooler temperatures moving southward from midlatitudes (Fig. 3d). It led to a temperature drop from ~285 to ~275 K over central China. Such an intrusion of low-tropospheric cold air resulted in an increased temperature gradient (i.e., frontogenetic processes) particularly in western-central China (Fig. 3b), which may help to produce moderate precipitation (Li et al. 2008b; Ding and Wang 2008; Li and Yu 2014).

Figures 4a–e show the spatial patterns of the low-level winds and the observed rainfall associated with the daily evolution of large-scale conditions. On 26–27 October, the southwesterly wind strengthened on the northwestern flank of the anticyclonic circulation (A1). The wind speed exceeded 12 m s^{-1} at 850 hPa and formed a low-level jet (LLJ) (Ding 1992; Liu et al. 2012), which coincided with heavy rainfall in eastern-central China (Figs. 4a,b). On 28 October, northerly wind appeared north of 32°N, coinciding with a southward-moving high pressure from higher latitudes. The northerly wind met the southwesterly flow and thus formed a west–east-oriented shear line (front) in central China, producing rainfall along the front (Fig. 4c). On 29–30 October, the anticyclonic circulation with low temperature (A2) dominated southeastern China where it replaced the previous one with high temperature (A1). As a result, the easterly wind prevailed over central China, and rainfall occurred west of 115°E (Figs. 4d,e). The WRF simulation reasonably reproduces the spatial patterns and daily evolution of the low-level circulation and rainfall (cf. Figs. 4f–j and 4a–e). The WRF simulation overestimates the rainfall on 26–27 October with southwestward displacement, probably due to an overestimation of LLJ and convergence in the 9-km-mesh model (Du et al. 2014; Chen et al. 2017). Nevertheless, the WRF Model reasonably reproduces the southwesterly LLJ and its shift to easterly wind, which are associated with the warm anticyclonic circulation (A1) and the replacement by the cold one (A2).

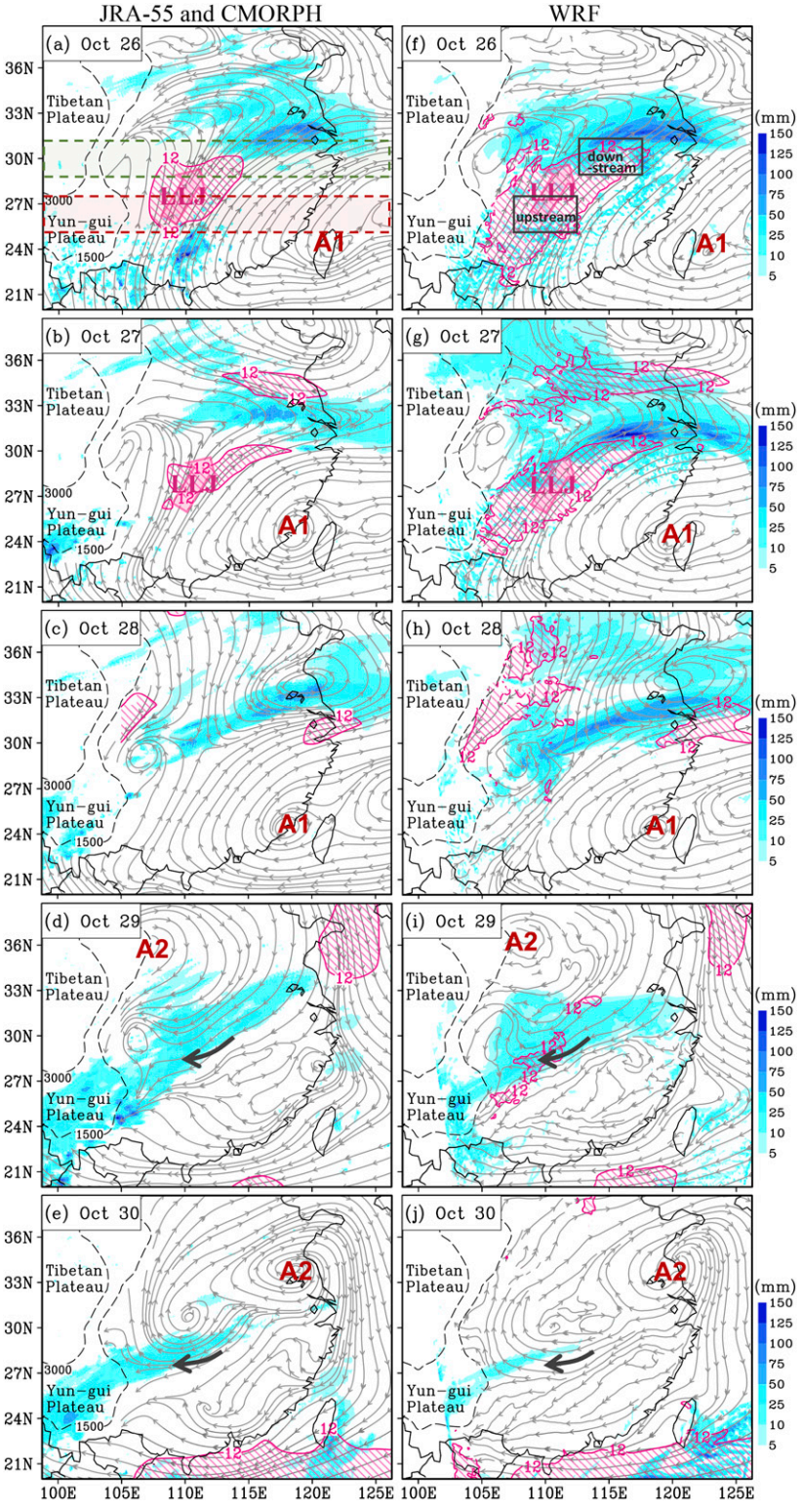

FIG. 4. (left) Daily mean of 850-hPa streamlines in the JRA-55 and rainfall in the CMORPH and (right) all of these in the WRF result. The 850-hPa wind speed exceeding 12 m s^{-1} is hatched in red. The anticyclonic circulations are marked by "A1" and "A2." Red arrows denote the LLJ in (a),(b),(f),(g), and black arrows denote the easterly wind in (d),(e),(i),(j). The zonal boxes in (a) show the areas to make Fig. 5. The rectangles in (f) show the upstream and downstream regions of the LLJ.

We further examine the diurnal variations of low-level winds under the changing large-scale conditions. Figure 5a shows that the southerly wind prevailed in southern China on 24–27 October and decayed after 28 October, as is shown in Figs. 4a–e. The southerly wind exhibited large diurnal variations on 26–27 October with an amplitude of ~2 m s^{-1}, while its diurnal variations became small after 28 October when the lower troposphere was cold. On 26–27 October, the southerly wind speed increased around midnight and reached a maximum of more than 12 m s^{-1}. It was followed by an enhanced westerly wind component in the downstream area (central China) that maximized during the morning hours (Fig. 5b). Such an enhancement in southeasterly wind led to formation of the NLLJ, which corresponded to the MCSs that developed in eastern-central China at night. The large diurnal variations of low-level winds seem to form over southern China and then extend downstream to central China, regulating rainfall systems, especially during the first half period under relatively warm conditions.

Figures 5c and 5d show that the WRF Model reasonably reproduces both the daily evolution and diurnal cycle of low-level wind components in the 8-day period. In particular, it captures the two NLLJs associated with MCSs on 26–27 October with more details than reanalysis. The WRF Model shows a wind speed stronger than JRA-55, which is likely due to higher spatiotemporal resolutions (Chen et al. 2017; Zhu et al. 2018). Nevertheless, the WRF reasonably reproduces the wind diurnal variations associated with the change in synoptic conditions. We also verified the WRF results that were regridded to the same resolutions as the JRA-55 and confirmed their overall consistency (not shown). In the following sections, we apply the high-resolution results of the WRF to examine the connection of MCSs to wind diurnal variations and their responses to the change in synoptic conditions.

4. Mechanisms governing the diurnal variations of low-level winds under changing large-scale conditions

a. *Diurnal variations in geostrophic and ageostrophic wind components*

As shown in section 3, the diurnal variations of low-level winds changed with the large-scale atmospheric conditions and exhibited a close association with rainfall. Here, we further examine the physical processes that govern the diurnal variations of low-level winds and their evolution with large-scale conditions. Previous studies have noted that the pressure gradient due to differential heating of terrain is a possible driving force of the diurnally varying winds, which is manifested as changes in the geostrophic component of wind (Holton 1967; Parish and Oolman 2010). Another factor may involve the inertial oscillation (clockwise rotation) of low-level winds induced by the diurnally varying frictional effect of turbulent mixing in the atmospheric boundary layer (ABL), which is manifested by the ageostrophic wind component (Blackadar 1957; Van de Wiel et al. 2010; Du and Rotunno 2014). To estimate the relative importance of these two factors, we decompose the low-level winds into geostrophic and ageostrophic components and examine their diurnal variations.

Because the diurnal variations of low-level winds had a spatial scale of several hundred kilometers as shown in Fig. 4a, we focused on the mesoscale features rather than synoptic or convective scales. Therefore, we use a low-pass Barnes filter on geopotential height to gain the geostrophic-scale motion (Barnes 1964). Then, we obtain the mesoscale ageostrophic motion by subtracting the geostrophic motion from the unfiltered motion. A recent study by Xue et al. (2018) has applied such a filtering method to study the physical mechanism of low-level winds under a relatively persistent large-scale circulation over East Asia. Following previous studies, we applied a spatial radius of ~150 km and other parameters similar to that of Xue et al. (2018) in the filtering algorithm. As a result, the geostrophic-scale motion with a wavelength larger than 1000 km was estimated by the filtered geopotential height. The ageostrophic wind component was derived by subtracting the geostrophic wind component from the unfiltered wind.

Figures 6a–d show that on the warm days, the geopotential height was larger in the southeast than in the northwest, in association with the WPSH. Such a geopotential pattern induced a southwesterly geostrophic flow. The geostrophic wind speed was largest east of the Sichuan basin (29°N, 107°E) but to the northwest of the area of LLJ (cf. shading in Fig. 6b and red hatch in Figs. 4a,f). The geopotential height gradient was slightly enhanced from the afternoon to maximize at ~2000 LT due to daytime heating (Figs. 6a,b). As a result, the geostrophic southwesterly wind strengthened to ~12 m s^{-1} in the evening. However, it decreased to ~8 m^{-1} before late night when the LLJ attained a maximum wind speed (cf. Figs. 6c and 5c). The wind direction of geostrophic flow changed little because the diurnal range of the geopotential was much smaller than the daily mean value. Therefore, the diurnal variations of geostrophic southwesterly wind may be inadequate to explain the nocturnal speed-up of LLJ that shifted from southerly to westerly wind. Nevertheless, the geostrophic flow reached ~8.5 m s^{-1} around midnight in the area of LLJ and accounted for a part (~45%) of the LLJ speed. The along-LLJ geostrophic component thus contributes to a part of the LLJ intensity, but its contribution is somewhat smaller

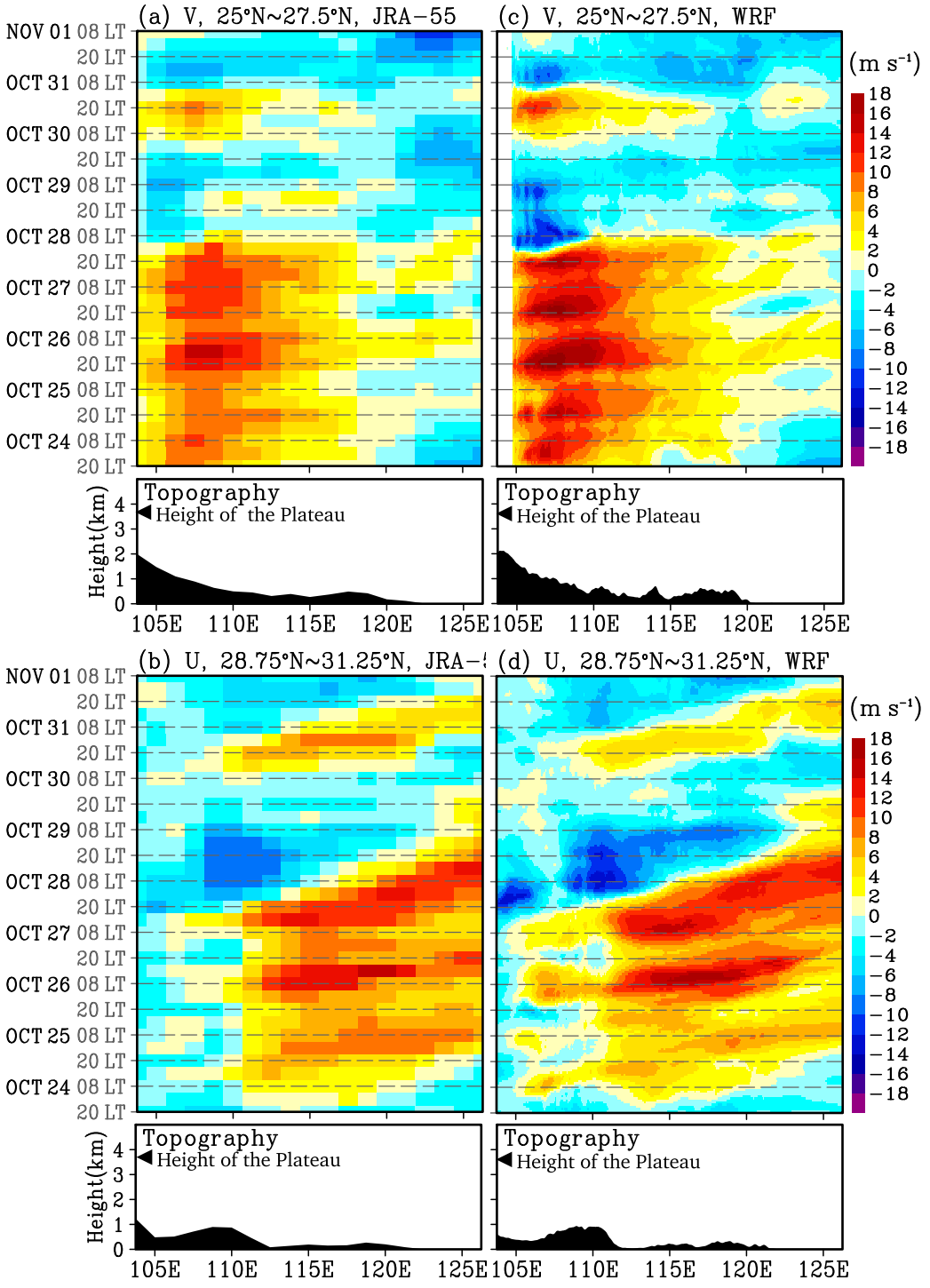

FIG. 5. Longitude–time diagrams of (a),(c) meridional wind ($m\,s^{-1}$) averaged in 25°–27.5°N and (b),(d) zonal wind ($m\,s^{-1}$) averaged in 28.75°–31.25°N, which were derived from (left) the JRA-55 reanalysis and (right) the WRF result. The zonal areas to make these figures are shown in Fig. 4a.

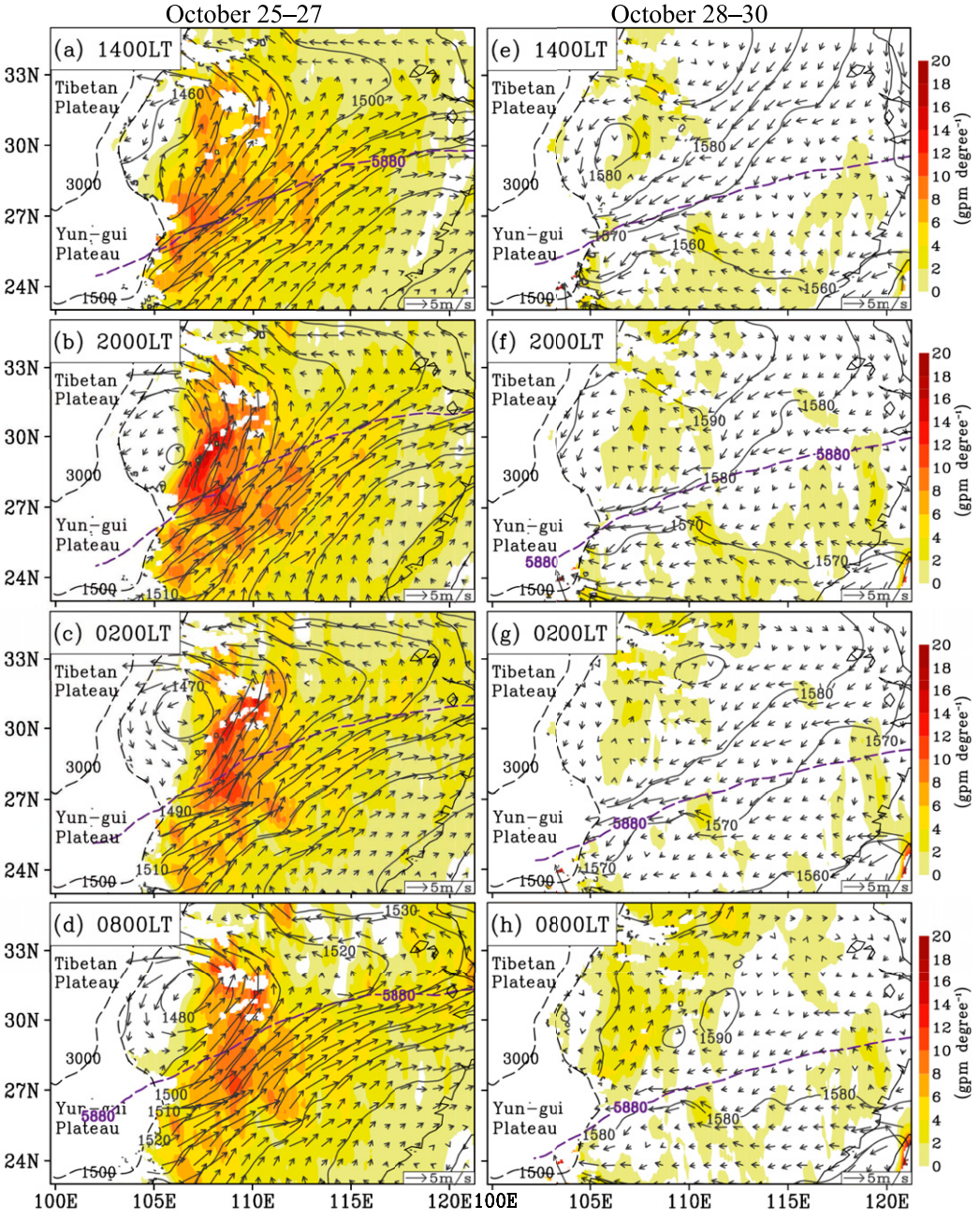

FIG. 6. The 6-hourly Barnes-filtered geopotential height (gpm, black contours) and its zonal gradient (gpm degree^{-1}, shading) as well as geostrophic wind (m s^{-1}, vectors) at 850 hPa. Composites of (a)–(d) 25–27 Oct and (e)–(h) 28–30 Oct. The purple dashed contours denote the 5880 gpm at 500 hPa, and the black dashed lines denote the elevations of 1500 and 3000 m. All these plots are derived from the WRF result.

than that in other studies (Parish and Oolman 2010; He et al. 2016; Shapiro et al. 2016). On cold days under the cold high (A2), the geostrophic easterly flow became prevalent over central China but its diurnal variation was negligible (Figs. 6e–h).

We then examine the diurnal variations of the ageostrophic wind component and their influence. Figures 7a–c show that during the first (warm) period, the ageostrophic wind exhibited large diurnal variations particularly near the eastern slopes of the Yun-gui Plateau. The deviated wind vectors exhibited a northeasterly anomaly in the afternoon (green), southeasterly anomaly in the evening (blue), southwesterly anomaly at late night (red), and northwesterly anomaly in the morning (purple).

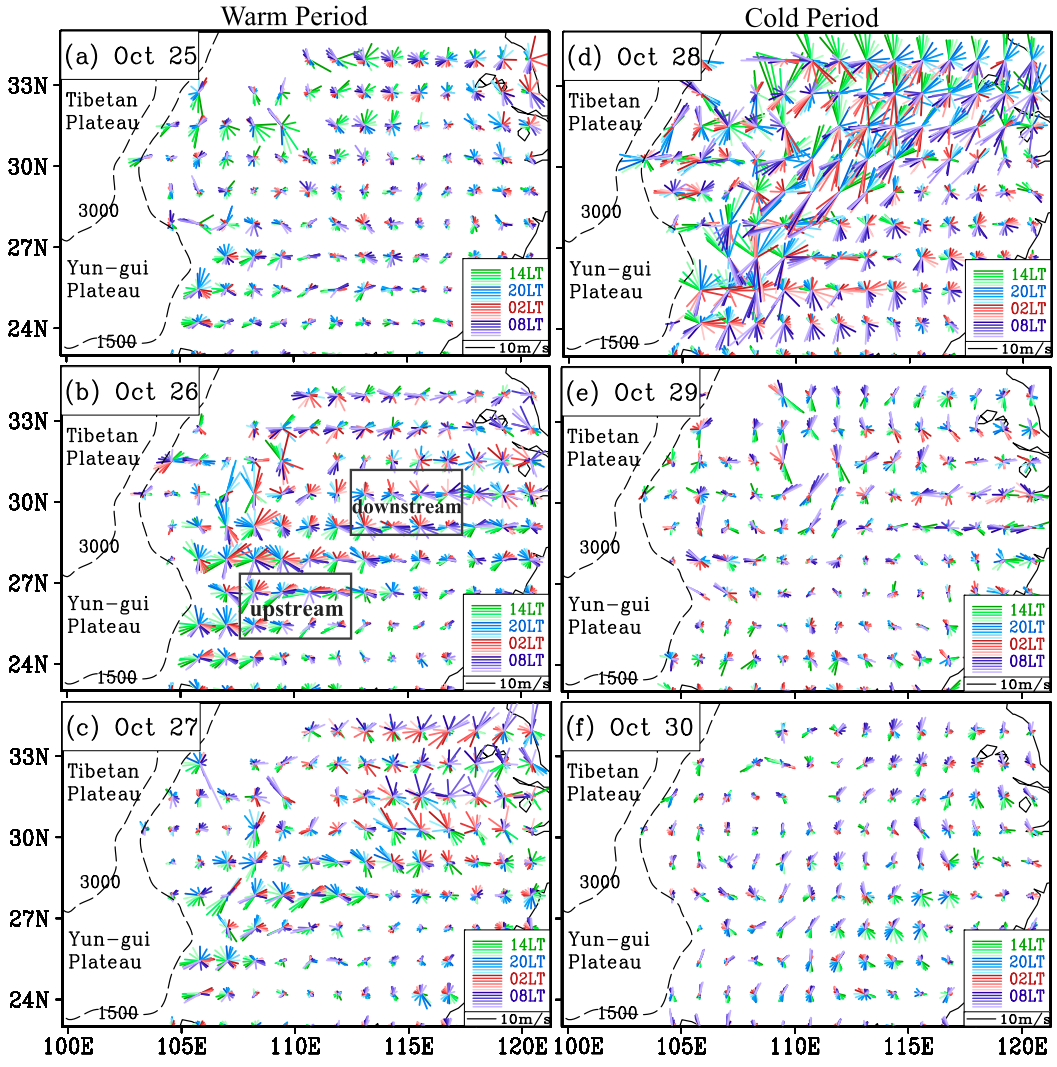

FIG. 7. Hourly deviation of 850-hPa ageostrophic wind ($m\,s^{-1}$) with the daily mean removed. The rectangles in (b) show the upstream and downstream regions of the LLJ for making Figs. 8–10. The black dashed lines denote the elevations of 1500 and 3000 m. All these plots are derived from the WRF result.

Such a clockwise rotation in ageostrophic wind direction seemed to be a response to the inertial oscillation (Blackadar 1957; Van de Wiel et al. 2010). The diurnal amplitude of ageostrophic wind reached up to ~5 $m\,s^{-1}$, which was larger than that of the geostrophic wind (~2 $m\,s^{-1}$). The late-night enhanced southwesterly ageostrophic wind was well superimposed on the background geostrophic flow, leading to the formation of NLLJ on 26–27 October. The clockwise rotation of ageostrophic wind may also explain the shifting direction of LLJ from southerly at night to westerly wind in the early morning. Such a large diurnal variation of ageostrophic wind and its contribution to the NLLJ are also observed in other warm-season studies (Chen et al. 2009b; Du et al. 2014; Xue et al. 2018; Zhang et al. 2019).

We also note that the diurnal variation of the ageostrophic wind did change in days. The amplitude was relatively small on 25 October and enhanced on 26–27 October (Figs. 7a–c), in association with the strengthening WPSH that led to a relatively warm condition in the lower troposphere (Fig. 3). The winds exhibited large diurnal variations mainly in meridional (zonal) wind component in the southwestern (northeastern) area, which corresponded to the speed-up of the southerly (westerly) wind as shown in Fig. 5. In particular, the downstream extension of the NLLJ on 26–27 October seemed to facilitate the growth of nocturnal MCSs in eastern-central China. On 28 October, wind vectors still experienced clockwise rotation at night in the warm area south of 27°N, but they varied inversely in higher latitudes due to the

incoming cold high pressure system (Fig. 7d). The diurnal amplitude of ageostrophic wind nearly disappeared on 29–30 October under the background easterly wind and cold conditions (Figs. 7e,f and 4i,j). Climatological studies have noted the difference in wind diurnal variations between warm and cold seasons (Yu et al. 2009; Chen et al. 2014). Here, we see a sudden decline in diurnal amplitude in a matter of days when atmospheric conditions shifted from a warm to cold scenario.

b. *Governing processes of the diurnally varying low-level winds*

To gain more insight into the forcings of wind diurnal variations, we analyze the momentum budget in this section. The momentum equation for the tendency of meridional wind component (v) and zonal wind component (u) is given below:

$$\frac{\partial \mathbf{V}}{\partial t} = -\mathbf{V}_h \cdot \nabla_h \mathbf{V} - \omega \frac{\partial \mathbf{V}}{\partial P} - \nabla \phi - f\mathbf{k} \times \mathbf{V} + \mathbf{F}_r. \quad (1)$$

The parameters of $\mathbf{V}$, P, ϕ, and f are the horizontal winds, pressure, geopotential, and Coriolis coefficient, respectively. The term on the left-hand side of Eq. (1) is the tendency of winds. The terms on the right-hand side are the horizontal momentum advection (ADV_h), vertical momentum transport (ADV_w), pressure gradient force (PGF), Coriolis force (CF), and frictional effect of ABL turbulent mixing ($\mathbf{F}_r$), respectively. The estimation of these terms in Eq. (1) can be obtained by the hourly output from the WRF simulation. The $\mathbf{F}_r$ term is derived as the residual of the other terms, which may be influenced by subgrid-scale processes. As shown in Figs. 5 and 7, the NLLJ seemed to establish near the east lee of the Yun-gui Plateau and then extended downstream into eastern-central China. Thus, we focus on the momentum budget over these key regions to clarify the dynamics of the NLLJ (see rectangles in Figs. 4f and 7b).

Figure 8a shows that in the upstream region of the LLJ, the southerly wind exhibited a regular speed-up from afternoon to midnight during 25–28 October (black solid). The acceleration had a maximum rate ranging from 0.8 to 1.4 $\mathrm{m\,s^{-1}\,h^{-1}}$. It was primarily driven by ageostrophic processes due to an imbalance (shading) between Coriolis force and pressure gradient force. Coriolis force underwent large diurnal variations (green dash) under an increasing pressure gradient (purple dash) on these days. Southerly acceleration maximized in the early evening (~2000 LT) when Coriolis force ($-fu$) reached its smallest in magnitude due to suppressed zonal wind. Meanwhile, the frictional drag of southerly wind declined dramatically after sunset and remained near zero through night because of the decayed turbulent mixing (red solid). Thus, the boundary layer flow decoupled with the surface at night, which allowed for a pressure gradient force exceeding Coriolis force to drive the southerly speed-up. The daily mean pressure gradient force increased from 25 to 26 October, which might amplify the diurnal-scale imbalance between pressure gradient force and Coriolis force. Therefore, the larger geostrophic wind explains the larger magnitude of the diurnally varying ageostrophic wind since previous studies have shown them to be proportional (Xue et al. 2018), and herein, we explicitly verify this relationship. Near midnight (~2400 LT), southerly acceleration rate declined to zero (Fig. 8a), and the southerly wind speed reached its maximum (Fig. 5b). The southerly wind turned to decelerate with a declined meridional ageostrophic imbalance after midnight when the increasing westerly wind speed enhanced the magnitude of Coriolis force ($-fu$).

Figure 8b shows that the westerly wind underwent acceleration during the nighttime hours on 25–28 October (black solid). The acceleration rate reached its maximum at ~2400 LT, with a lag of ~4 h from that of the southerly wind. The westerly acceleration was driven by the imbalance (shading) between the diurnally varying Coriolis force and the relatively persistent pressure gradient force. The strongest westerly acceleration around midnight was explained by the largest Coriolis force (fv) (Fig. 8b) with the maximum southerly wind speed (Fig. 8a). The westerly acceleration ended at ~0800 LT because of frictional drag (red solid), and the maximum westerly wind speed contributed to the southerly deceleration ($-fu$), as shown in Fig. 8a. Therefore, the nocturnal speed-up of westerly wind followed the preceding speedup of southerly wind that was essentially driven by the ageostrophic processes due to the diurnally varying friction. In this respect, the resultant clockwise rotation of the deviated wind vectors matched the prediction of the Blackadar's theory of boundary layer inertial oscillation (Blackadar 1957). Previous studies also recognized the inertial oscillation as the major process driving the wind diurnal variations over southern China (Chen et al. 2009b; Du et al. 2014; Xue et al. 2018). Here, this study further highlights that the strong inertial oscillation due to the diurnally varying friction drag can increase with the magnitude of background southwesterlies. Notably, the horizontal advection term became negative after midnight (blue solid in Figs. 8a,b), suggesting a momentum outflow in the upstream region of LLJ. As a comparison, when cold air dominated on 29–31 October, all terms of the momentum equation decayed in magnitude (Figs. 8a,b). Their diurnal cycles nearly vanished, and thus, the diurnal variations of low-level winds became negligible.

We further examine the dynamics of low-level winds in the downstream region of LLJ. Figure 8c shows that the southerly wind accelerated from evening to late night

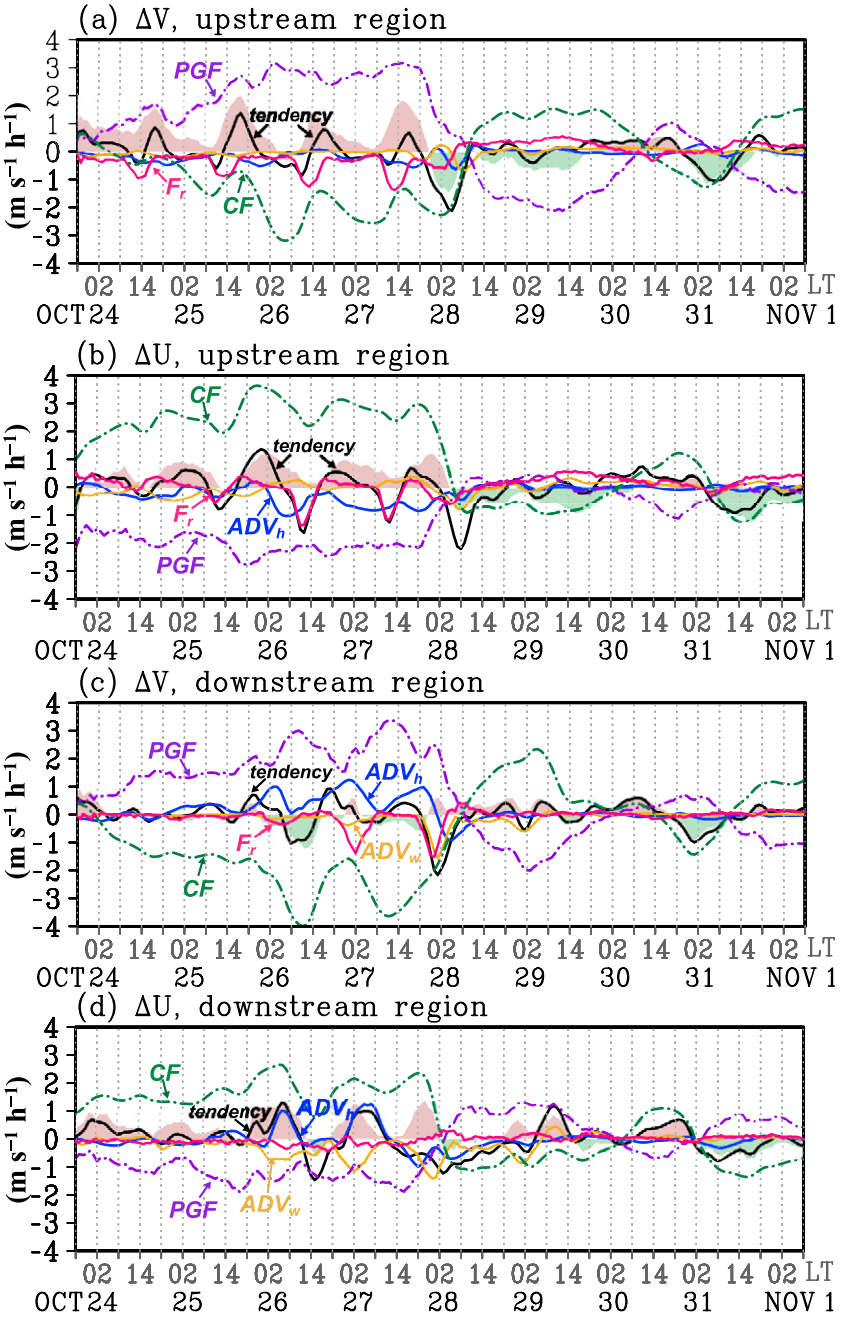

FIG. 8. Momentum budget for 850-hPa meridional wind (v) and zonal wind (u) over the (a),(b) upstream region and (c),(d) downstream region of the LLJ. The black line denotes the tendency of winds on the left-hand side of Eq. (1). The purple line, green line, red line, blue line, and yellow line denote pressure gradient force (PGF), Coriolis force (CF), Frictional effect ($\mathbf{F}_r$), horizontal momentum advection (ADV_h), and vertical momentum transport (ADV_w), respectively. The shading denotes the sum of the PGF and CF. All these plots are derived from the WRF result.

on 26–28 October (black solid). The acceleration rate reached a maximum of 0.8–1.0 m s^{-1} h^{-1} near midnight, with a delay of 2–3 h compared to that in the upstream region. Because the imbalance between Coriolis force and pressure gradient was small or negative (shading), the southerly acceleration was not locally driven by the boundary layer inertial oscillation, and the reason will be discussed later. Instead, the horizontal momentum advection term became largely positive near midnight (blue solid) and thus contributed greatly to the southerly acceleration. The vertical momentum transport and friction terms became negative during the predawn hours, which acted to decelerate the southerly wind (yellow and red solids). As a result, the southerly acceleration ended and the southerly wind speed maximized at late night in the downstream region.

Figure 8d shows that the downstream westerly acceleration maximized after ~0200 LT 27–28 October, with a lag of ~4 h from the southerly acceleration. This maximization was partly driven by the ageostrophic process (shading) due to the enhanced Coriolis force, which acted to accelerate the westerly wind by veering the southerly wind. The acceleration was largely contributed by the horizontal advection of zonal wind momentum after midnight (blue solid). Therefore, the acceleration of the westerly wind had a stronger intensity and longer duration than that of the southerly wind, which explained the significant diurnal variations of zonal wind in the downstream area (Fig. 7). The westerly wind turned to decelerate in the morning when the Coriolis force and horizontal advection terms declined. As both the westerly and southerly accelerations strongly rely on horizontal momentum advection, the NLLJ in the downstream area (central China) may be built by the external forcing in the upstream area (southern China). Such a dominant effect of momentum advection was supported by the strong southwesterly wind on the northwestern flank of WPSH. It may explain why the NLLJ usually extends downstream from southern to central China with a prevalent southerly wind shifting to a westerly wind (Ninomiya 2000; Chen et al. 2017). Shin et al. (2019) noted a downstream growth of nighttime southwesterlies over the East China Sea but at an amplitude smaller than that found on land in this study. On 29–31 October, the diurnal variations of momentum advection were small for both southerly and westerly winds (Figs. 8c,d). This was probably due to relatively weak easterly wind over southern China under the cold high (Figs. 4i,j).

c. *Connection of large-scale conditions to diurnally varying regional forcings*

In this section, we first examine the influence of large-scale thermodynamic/dynamic conditions on the physical processes at diurnal time scale, such as the boundary layer inertial oscillation. Figure 9a shows that, on the warm days of 24–27 October, the near-surface temperature gradually increased, with a large diurnal range of up to ~8 K (solid). The temperature increase manifests as strong surface heating by shortwave radiation over southern China (Fig. 9e). The air temperature in the ABL also exhibited large diurnal variations with an afternoon maximum (dash), suggesting strong vertical turbulent mixing. As a result, the ABL height increased in the daytime and reached its highest value at ~1400 LT (Fig. 9b). Such strong turbulent mixing is thought to produce a large frictional drag that slowed down the westerly wind speed to induce an imbalance between Coriolis force ($-fu$) and pressure gradient force for southerly acceleration from afternoon (Fig. 8a). Then, the frictional drag on the meridional wind decayed after sunset to further maximize the southerly acceleration in the early evening. As strong surface heating tended to occur under low relative humidity and cloud-free conditions (Figs. 9c,d), the strengthening WPSH was conducive to a large inertial oscillation of low-level winds (Figs. 3a,c). The WPSH also led to strong southwesterlies on its northwestern flank, which promoted the diurnal amplitudes of Coriolis force and friction terms (Fig. 8a), thereby producing the large wind diurnal variations in southern China. As a comparison, the diurnal variation of surface heating was relatively weak in central China (Fig. 9a), because of the sustained cloudiness (Figs. 9d,e). In this area, wind diurnal variations were mainly attributed to the momentum advection by southwesterlies along the WPSH, so that they relied on the forcings in the upstream area rather than the local ones. Therefore, for the first time, this study highlights that the thermodynamic and dynamic conditions of a strong WPSH play a crucial role in driving the diurnal variations of low-level winds over China.

On cold days after 28 October, the air temperature exhibited small diurnal variations both near the surface and in the boundary layer (Fig. 9a). The ABL top in the upstream region stayed lower than 500 m during the cold period except on 30 October. The suppressed turbulent mixing corresponded to a weak influence of boundary layer inertial oscillation as shown in section 4b. These features were attributed to high relative humidity (Fig. 9c) and cloudy conditions (Fig. 9d) that reduced surface heating. Figure 9f shows that the clouds increased after 28 October, with its top extending to 400–500 hPa. The cloudiness seemed to form in the stratification with low-level cold air and midlevel warm moist air related to the remaining WPSH aloft (Figs. 3c,d). Therefore, the stably stratified and cloudy conditions due to cold air intrusion

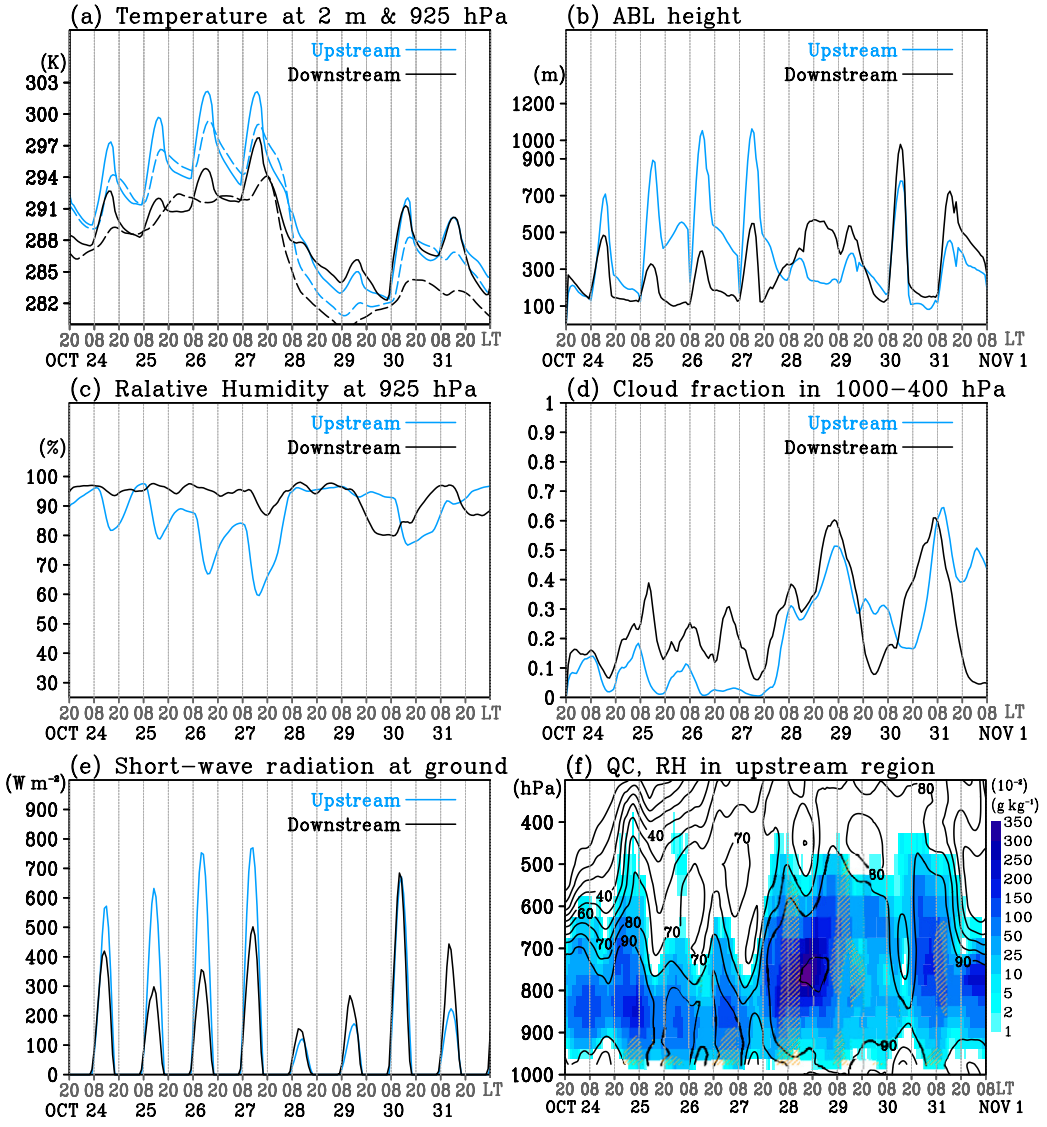

FIG. 9. Hourly variations of (a) temperature at 2 m above ground (K, solid) and at 925 hPa (K, dash), (b) ABL height (m), (c) relative humidity at 925 hPa (%), (d) cloud fraction averaged in the 1000–400 hPa layer, and (d) the shortwave radiation at the ground (W m^{-2}), averaged over the upstream region (blue line) and downstream region (black line) of the LLJ. (f) Time–vertical section of the cloud water mixing ratio (10^{-5} g kg^{-1}, shading) and relative humidity (%, contours) averaged over the upstream region. The yellow hatched area in (f) denotes the temperature deviation (where the daily mean value is removed) greater than 1 K. All these plots are derived from the WRF result.

were unfavorable to the ABL turbulent mixing and inertial oscillation.

In the presence of the cloudiness on cold days, the radiative forcings were suppressed near the surface and in the ABL, but they may be relatively strong at the cloud top. Figure 9d shows that the cloud fraction regularly increased after sunset and maximized near morning in the upstream region. Such nocturnal cloudiness well corresponded to enhanced cloud water, with particularly large diurnal cycles in the upper half of the cloudy layer (700–400 hPa), as shown in Fig. 9f. It was closely associated with the enhanced (suppressed) relative humidity at the cloud top, which coincided with the temperature perturbation due to radiative nighttime cooling (daytime heating). The negative temperature perturbation (hatched) in the upper part of the cloud might also have a destabilizing effect. Therefore, the regional radiative forcings were elevated to the cloud top, and their influence on humidity/condensation explained the nighttime peaks of stratiform precipitation on 29–31 October (Figs. 2b,d).

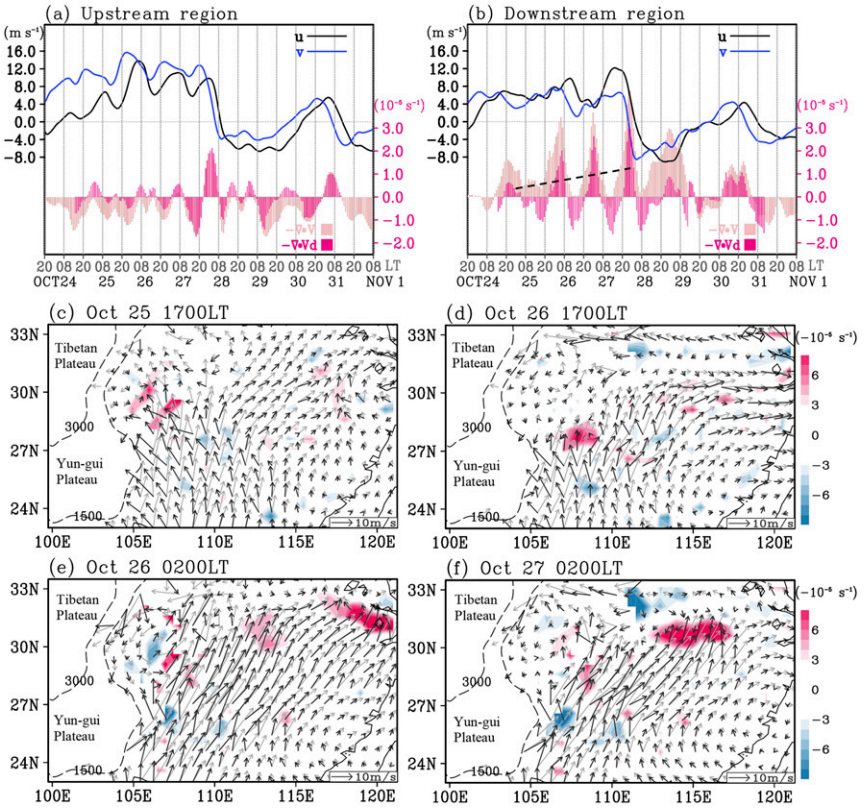

FIG. 10. Hourly variations of the 850-hPa meridional wind ($m\,s^{-1}$, blue line), zonal wind ($m\,s^{-1}$, black line), horizontal convergence (indicated as "$-\nabla \cdot V$," s^{-1}, pink bar), and the deviated horizontal convergence where the daily mean convergence has been removed (indicated as "$-\nabla \cdot Vd$," s^{-1}, red bar) in (a) the upstream region and (b) the downstream region. The long-dashed black line in (b) denotes the daily mean value of convergence during 24–27 Oct. The upstream and downstream regions are marked by rectangles in Figs. 7b and 4f. (c)–(f) Spatial distributions of the 850-hPa winds ($m\,s^{-1}$, gray vectors), ageostrophic wind ($m\,s^{-1}$, black vectors), and horizontal convergence (s^{-1}, shading). All these plots are derived from the WRF result.

Climate analyses have attributed the prevalent nocturnal precipitation to cloud-top cooling during the cold season when stratiform clouds prevail (Yu et al. 2004; Li et al. 2008b; Zhang et al. 2014; Huang and Chang 2018), and we now see that such a cloud-top cooling also enhances rainfall at night during the extreme rainfall event.

5. Impacts of wind diurnal variations on the development of nocturnal MCSs

a. Diurnal variations of horizontal convergence and water vapor flux

In this section, we examine how wind diurnal variations regulate the dynamic and thermodynamic processes that influence precipitation systems under changing large-scale conditions. We focus on the formation of MCSs at the predawn on 26–27 October under the warm scenario. First, we examine the horizontal convergence of low-level winds to show dynamical lifting conditions. Figure 10a shows that in the upstream region, divergence (pink bar) was dominant throughout the event as it was located at the entrance of LLJ or affected by the cold air. In contrast, Fig. 10b shows that strong convergence appeared in the downstream region of the southwesterly LLJ during the warm period. The daily mean convergence was gradually enhanced on 24–27 October (black dash), in association with the strengthening southwesterlies along with the enhanced WPSH. The convergence exhibited pronounced diurnal variations (red bar), with a diurnal amplitude comparable to its daily mean value. The largest convergence appeared at ~0200 LT 26–28 October, leading to the subsequent growth of MCSs during the predawn hours (Fig. 2a). The peak hours of convergence coincided with the late-night maximum of the southerly wind component (blue solid), suggesting that low-level ascent was enhanced downstream of the NLLJ. The convergence decayed and its diurnal cycle was suppressed after the intrusion of cold air on 28 October.

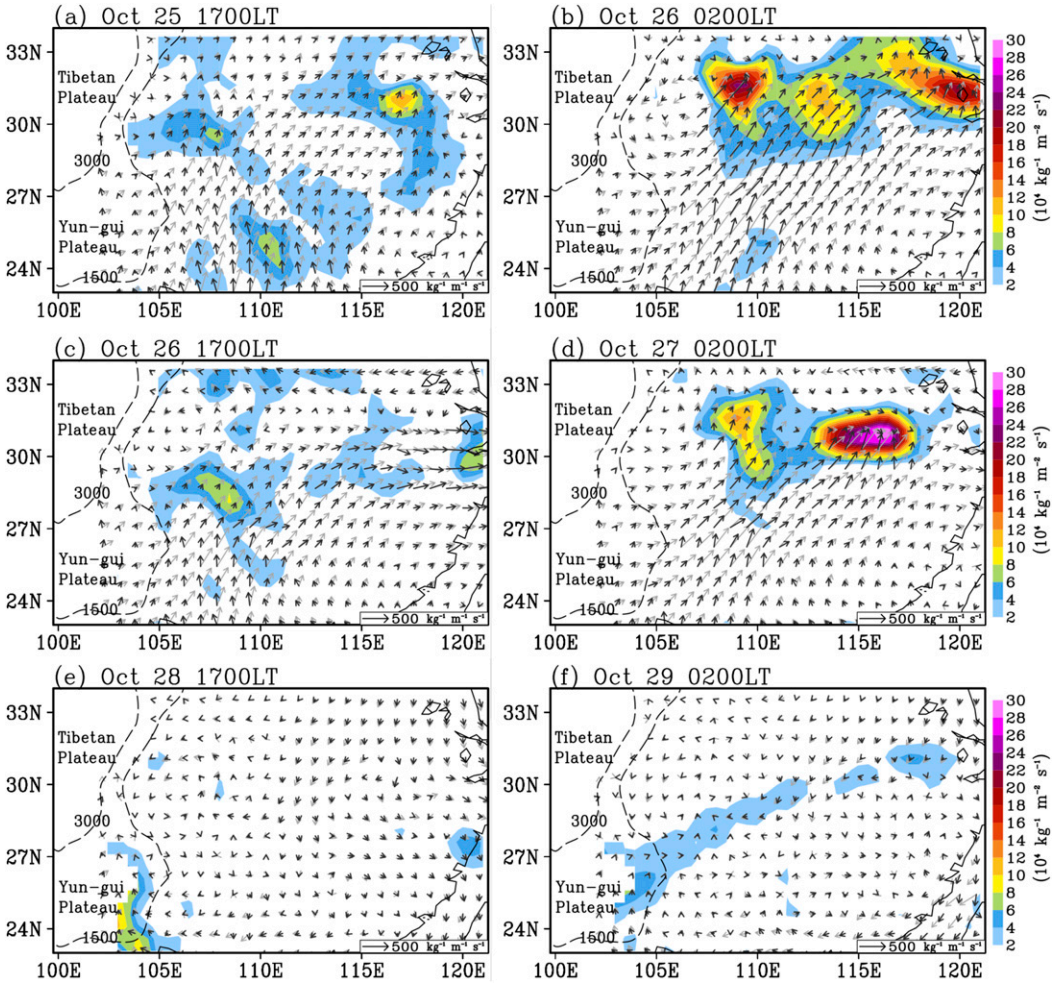

FIG. 11. Spatial distributions of the moisture flux by full winds ($kg\,m^{-1}\,s^{-1}$, gray vectors) and the horizontal moisture flux convergence (the sum of the horizontal moisture advection and specific humidity multiplied by the horizontal convergence, $10^4\,kg\,m^{-2}\,s^{-1}$, shading), and the moisture flux by ageostrophic wind ($kg\,m^{-1}\,s^{-1}$, black vectors). All of these fluxes are vertically integrated from the surface to 700 hPa and derived from the WRF result.

We next investigate the spatial pattern of ageostrophic wind to clarify the formation of convergence prior to the nocturnal MCSs on 25–27 October. Figures 10c and 10d show that in the afternoon, the ageostrophic wind over southern China were directed toward the northwest, roughly perpendicular to the background southwesterly wind. They induced weak convergence to eastern slopes of the plateau. Figures 10e and 10f show that at late night, the ageostrophic wind vectors rotated clockwise toward the northeast, roughly parallel to the background wind, leading to the formation of the southwesterly NLLJ. Strong convergence occurred downstream of the ageostrophic wind with mesoscale centers at ~118°E on 26 October and at ~113°E on 27 October, corresponded well to the locations of the MCSs as denoted by "A" and "B" in Fig. 2b. Such a synoptic-scale southwesterly wind that strengthened repeatedly at night over southern China and then triggered several mesoscale systems over central China, are also observed in warm seasons (Chen et al. 2017; Xue et al. 2018). Figures 10e and 10f also show that the diurnal variations of ageostrophic wind were strongest on the northwestern flank of the WPSH, where the relatively warm condition and large geostrophic wind were conducive to turbulent mixing and momentum advection, as shown in section 4. Therefore, the large-scale condition of an enhanced WPSH plays a key role in the strength of diurnally varying ageostrophic wind and its downstream impact on convergence, which may be regarded as a precursor to nocturnal MCSs (Augustine and Caracena 1994).

We further examine the diurnal variations of moisture flux and its convergence, which is one of the important factors for MCSs development (Banacos and Schultz 2005). Figures 11a and 11c show that the moisture flux and its convergence were relatively weak in the afternoon,

with spatial patterns similar to the low-level winds. Figures 11b and 11d show that the moisture flux convergence became strong at late night with several mesoscale maxima over central China, coinciding with the MCSs development. Such enhanced moisture flux convergence was mostly attributed to the ageostrophic moisture flux that rotated toward the northeast at late night. Recent studies noted that the ageostrophic wind played a leading role in regulating the diurnal variations of moisture flux and the resultant rainfall (Xue et al. 2018; Zhang et al. 2019). As the ageostrophic wind declined after 28 October, the moisture flux convergence weakened and mostly appeared in the eastern slopes of the Yun-gui Plateau and western-central China (Figs. 11e,f).

b. *Diurnal variations of moist static energy and convective instability*

We further examine the moist static energy and convective instability associated with the MCSs development. Figure 12a shows that the warm, moist air with high θ_e extended from southern China to central China during 24–27 October, in association with the strengthening WPSH. To the south of 28°N, the θ_e value increased significantly in the daytime and reached a maximum of ~355 K in the afternoon due to intense solar heating under less cloudy conditions, as mentioned in section 4c. Thus, the moist static energy increased during the daytime over southern China. As for central China (28°–31°N), the increase of θ_e value was much slower in the daytime because of the cloudy conditions. The θ_e maximum was delayed northward and appeared at late night near ~31°N. The moist static energy in central China seemed to depend on the transport from southern China, which coincided with the NLLJ that acted as an effective conveyor of moisture.

Figures 13a–d show the vertical structures of winds and moist energy on 25–27 October. At 1700 LT, the moist static energy accumulated to the south of 28°N, with a 1.5-km-depth layer of high θ_e under suppressed southerly wind (Figs. 13a,b). At 0200 LT, the southerly wind increased to ~10 m s^{-1} and the high-θ_e air moved northward and ascended along the tilted frontal surface at 28°–31°N. The θ_e value increased by ~6 K in the 1-km layer above ground at ~30°N (Figs. 13c,d). The θ_e advection associated with the NLLJ provided elevated instability in the frontal zone, thereby contributing to the MCSs activity (Trier et al. 2014; Chen et al. 2017). This feature highlights that such a daytime charge of energy in southern cloud-free zone and a nighttime discharge in northern frontal zone by NLLJ are a key MCS-bearing process in warm scenario, which may be more generalized to the other cases in the mei-yu season (Shinoda et al. 2005; Yamada et al. 2007).

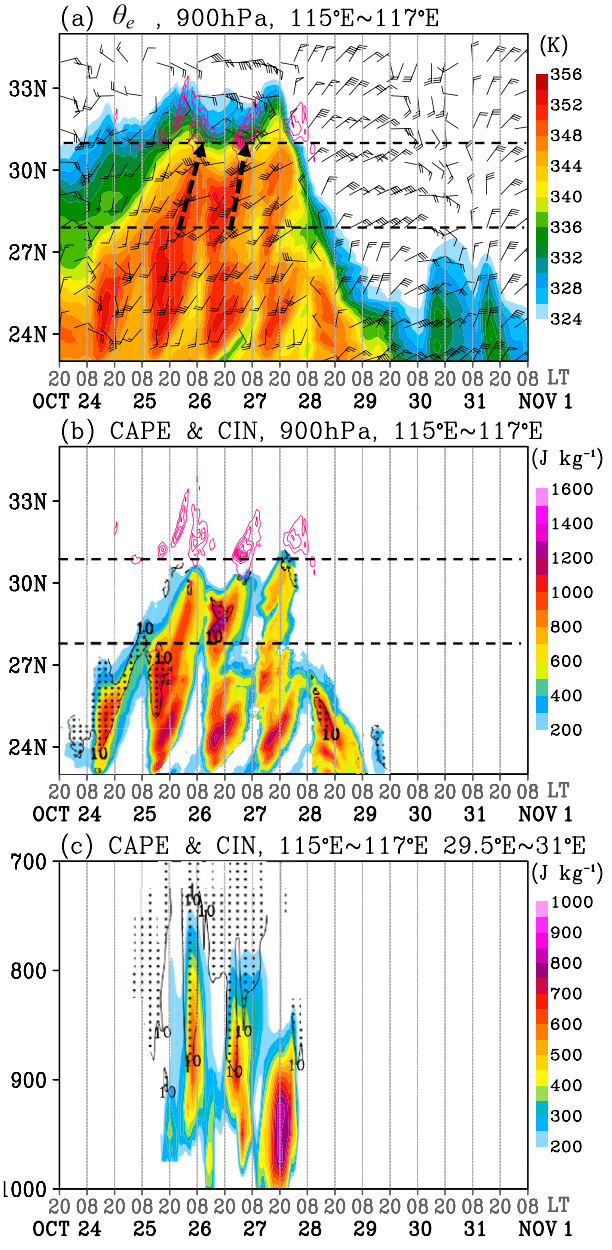

FIG. 12. Time–latitude diagrams of 900-hPa (a) equivalent potential temperature (K, shading) and (b) CAPE (J kg^{-1}, shading) and CIN (J kg^{-1}, dots) averaged over 115°–117°E. The barbs show the 900-hPa winds (m s^{-1}), with short and long barbs denoting wind speeds of 2 and 4 m s^{-1}, respectively. Rain rate greater than 2 mm h^{-1} is contoured in red. The black dashed line denotes the latitudes of 28° and 31°N, and the black dashed arrows denote the northward transportation of high-θ_e air. (c) Vertical–time section of CAPE (J kg^{-1}, shading) and CIN (J kg^{-1}, dots) averaged in the frontal area (29.5°–31°N, 115°–117°E). All these plots are derived from the WRF result.

Figure 12b shows that the CAPE experienced diurnal variations similar to θ_e on 24–27 October. The CAPE increased in the southern area during daytime, while it exhibited a delayed maximum during the predawn hours

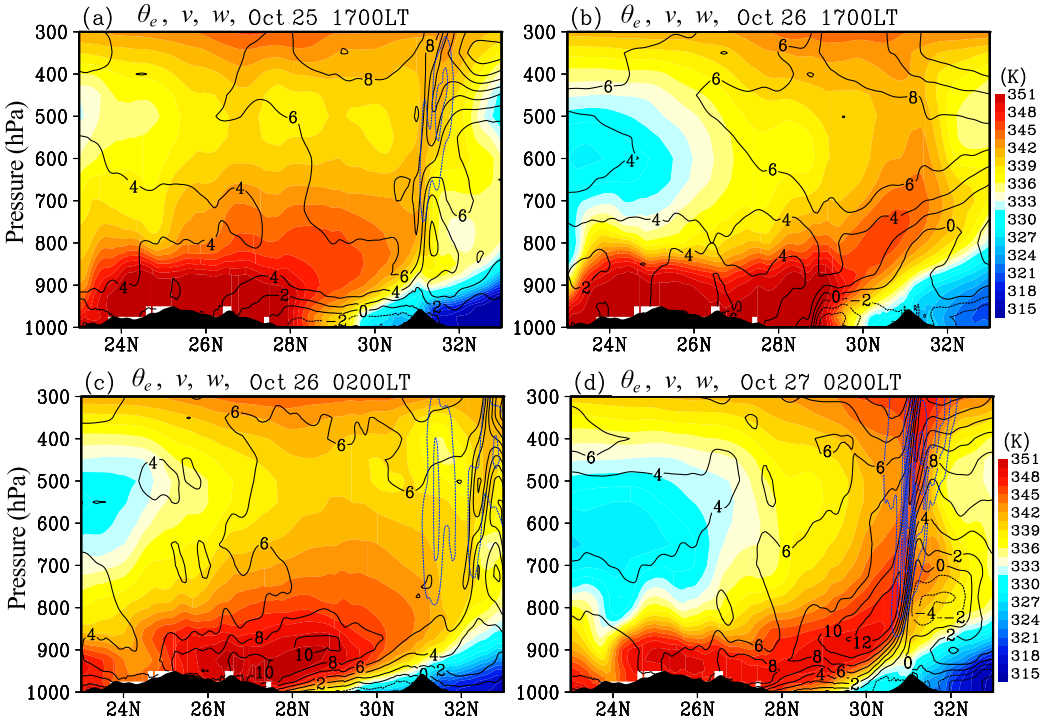

FIG. 13. Latitude–vertical sections of equivalent potential temperature (K, shading), meridional wind ($m\,s^{-1}$, black solid), and the following 6-h mean of upward motion greater than $0.1\,m\,s^{-1}$ (blue dash) averaged over 115°–117°E. All these plots are derived from the WRF result.

at 28°–31°N, in phase with the northward movement of high-θ_e air. This feature indicates that the horizontal advection of warm moist air by the NLLJ contributed greatly to the CAPE generation in central China. Notably, the high-θ_e air was lifted up in the frontal zone (Figs. 13c,d), and thus, the vertical transport of moisture might produce an additional part of CAPE. Overall, the NLLJ played a crucial role in generating a moderate CAPE of ~$700\,J\,kg^{-1}$ and reduced the CIN to below $5\,J\,kg^{-1}$ at an elevated layer in the early morning of 26–27 October (Fig. 12c). Such an elevated convectively unstable inflow with enhanced lifting led to convection initiation in the frontal zone as shown by red contours in Figs. 12a and 12b. Therefore, the influence of NLLJ on triggering nocturnal MCSs, which is usually observed in the warm season (e.g., Trier et al. 2014, 2017; Chen et al. 2017), is also applicable for the warm scenario in late October. The NLLJ seems to express a downscaling influence of large-scale atmospheric conditions on mesoscale systems.

During the second half period after 28 October, the lower troposphere was affected by an intrusion of cold air (Fig. 3b), while the warm moist energy decayed (Figs. 12a,b). The rainfall systems mainly developed over western-central China (Fig. 2). In this area, the rainfall was probably supported by the frontogenetic processes with an increased temperature gradient (Fig. 3b) and the upslope lifting by low-level easterly wind (Fig. 4i). These two processes were mainly at the daily time scale, while the nighttime rainfall peak may be partly attributed to the increased relative humidity as a result of the cloud-top radiative cooling as discussed in section 4c.

6. Conclusions and discussion

In this study, we investigate how changing large-scale atmospheric conditions influence mesoscale rainfall systems through diurnally varying processes during a long-lived heavy rainfall event. The major findings are listed as follows:

1) The extreme heavy rainfall that occurred in central China during 24–31 October 2016 underwent two different stages of diurnal cycles in response to the changing large-scale conditions. During 24–27 October, intense convective rainfall was mainly recorded in eastern-central China with a morning peak. The rainfall was closely associated with the establishment of the southwesterly NLLJ in southern China and its downstream influence in central China, corresponding to an enhanced WPSH. During 28–31 October, moderate rainfall systems occurred in western-central China and mostly maximized at the predawn.

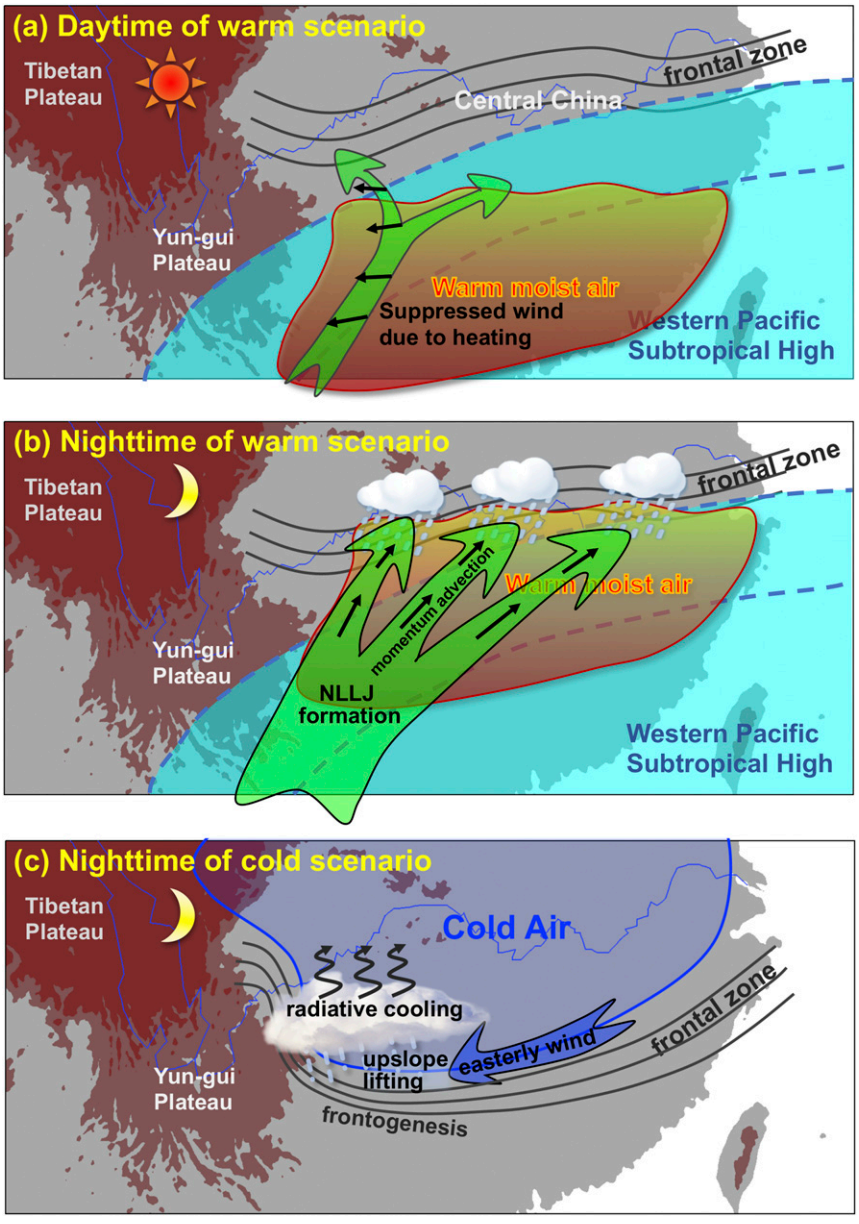

FIG. 14. Conceptual model of the rainfall-producing processes in (a) daytime and (b) nighttime of the warm period and (c) nighttime of the cold period. The light blue area denotes the WPSH in (a),(b). The bold arrows denote the low-level winds with the black vectors denoting their diurnal deviations. The red area in (a),(b) denotes the warm and moist air mass, while the dark blue area in (c) denotes the cold air with high pressure. The nocturnal MCSs in the frontal zone are marked in (b). The clouds and rainfall are marked in (c).

The shift in precipitation was related to the decayed wind diurnal variations due to an intrusion of low-tropospheric cold air from midlatitudes. The WRF simulation reasonably reproduced the diurnal cycle of rainfall patterns (locations, peak hours) and their shifts with the changing large-scale conditions.

2) Momentum analyses show that the nocturnal speed-up of the southwesterly LLJ during the warm period originated in southern China. The southerly wind component over southern China peaked near midnight and the westerly wind maximum followed at the predawn, in association with the clockwise rotation of ageostrophic wind. Such wind diurnal variations were found to respond to the diurnally varying frictional effect of ABL turbulent mixing, which matches the prediction of the Blackadar's inertial oscillation

theory. In the downstream area (central China), the NLLJ was established during the predawn hours mostly by the acceleration in westerly wind component. The acceleration was attributed to the advection of horizontal momentum from southern China. The WPSH not only provided cloud-free conditions in southern China favoring a strong Blackadar's inertial oscillation but also strengthened the background southwesterlies favoring the momentum transport to central China, resulting in a downstream extension of the NLLJ. In the second period, the diurnal variations of low-level winds decayed as the lower troposphere became cold and was dominated by easterly wind.

3) The southwesterly NLLJ contributed greatly to the growth of nocturnal MCSs in eastern-central China on 25–27 October. The NLLJ strengthened the horizontal convergence at its northeastern terminus, with mesoscale centers coinciding with the growth of MCSs. The NLLJ possessed a feature of ageostrophic wind that led to enhanced moisture flux convergence. The NLLJ also served as a nighttime conveyor of warm moist air from southern China where the high-θ_e air mass was built up in a 1.5-km-depth layer during the daytime. The warm moist air ascended along the tilted frontal surface over central China, where it produced convective instability with moderate CAPE and small CIN that favored nocturnal convection growth. After 29 October, the convergence became suppressed with the decayed wind diurnal variations. The rainfall with a predawn peak occurred in western-central China, which may be induced by the enhancement of frontogenetic processes, upslope lifting and cloud-top radiative cooling.

Based on these results, we conclude that the transition of large-scale conditions from warm to cold scenarios can influence the timing and location of rainfall systems by regulating diurnal variations. A conceptual model is proposed to summarize the related processes. Figure 14a shows that when the WPSH is enhanced over southeastern China, the daytime heating over cloud-free areas increases the moist static energy in the lower troposphere (Yamada et al. 2007; Chen et al. 2017). The heating also induces vertical turbulent mixing in the ABL, controlling the strength of wind diurnal variations (Xue et al. 2018). When the turbulent mixing decayed at night, the southwesterly NLLJ forms in southern China (Fig. 14b). It extends to central China with the help of background southwesterlies on the northwestern flank of the WPSH (Shin et al. 2019). From a dynamic perspective, the WPSH seems to modulate both the strength and extending direction of wind diurnal variations. From a thermodynamic perspective, the WPSH is conducive to a daytime charge of moist static energy in southern China and a nighttime discharge to eastern-central China. Thus, the WPSH favors the growth of morning-peak MCSs in the frontal zone. Figure 14c shows that under the cold scenario, the wind diurnal variations become suppressed, while the frontogenetic processes and the upslope lifting of easterly wind are evident in western-central China where rainfall systems develop. The rainfall tends to maximize at predawn likely due to the nighttime cloud-top cooling that increases the relative humidity. This study is one of the first studies to show that such a process downscaling from large-scale to mesoscale may change under shifting atmospheric conditions over East Asia, which can be used to evaluate numerical models for the prediction of severe heavy rainfall. Our ongoing work involves studying more rainfall events using climate simulations at convection-permitting resolutions (Satoh and Kitao 2013; Zhu et al. 2018; Li et al. 2018). Further analyses help to clarify the physical process downscaling from large-scale conditions to mesoscale systems and its role in regional climate and extreme weather (Wang et al. 2014; Trier et al. 2014).

Acknowledgments. The authors thank the editor, Prof. David M. Schultz, and four anonymous reviewers for their constructive suggestions. The authors are grateful to NOAA/CPC for providing the CMORPH data, to JMA for providing the JRA-55 reanalysis data, and to NASA for providing the FNL data. This work is supported by the National Key Research and Development Program of China (Grant 2016YFA0600704) and the National Natural Science Foundation of China (Grants 41575068, 41875055, and 41530530).

REFERENCES

Augustine, J. A., and F. Caracena, 1994: Lower-tropospheric precursors to nocturnal MCS development over the central United States. *Wea. Forecasting*, **9**, 116–135, https://doi.org/10.1175/1520-0434(1994)009<0116:LTPTNM>2.0.CO;2.

Banacos, P. C., and D. M. Schultz, 2005: The use of moisture flux convergence in forecasting convective initiation: Historical and operational perspectives. *Wea. Forecasting*, **20**, 351–366, https://doi.org/10.1175/WAF858.1.

Bao, X., F. Zhang, and J. Sun, 2011: Diurnal variations of warm-season precipitation east of the Tibetan Plateau over China. *Mon. Wea. Rev.*, **139**, 2790–2810, https://doi.org/10.1175/MWR-D-11-00006.1.

Barnes, S. L., 1964: A technique for maximizing details in numerical weather map analysis. *J. Appl. Meteor.*, **3**, 396–409, https://doi.org/10.1175/1520-0450(1964)003<0396:ATFMDI>2.0.CO;2.

Blackadar, A. K., 1957: Boundary layer wind maxima and their significance for the growth of nocturnal inversions. *Bull. Amer. Meteor. Soc.*, **38**, 283–290, https://doi.org/10.1175/1520-0477-38.5.283.

Cai, Y., X. Lu, G. Chen, and S. Yang, 2018: Diurnal cycles of Mei-yu rainfall simulated over eastern China: Sensitivity to cumulus convective parameterization. *Atmos. Res.*, **213**, 236–251, https://doi.org/10.1016/j.atmosres.2018.06.003.

Carbone, R. E., and J. D. Tuttle, 2008: Rainfall occurrence in the U.S. warm season: The diurnal cycle. *J. Climate*, **21**, 4132–4146, https://doi.org/10.1175/2008JCLI2275.1.

Chen, G., W. Sha, and T. Iwasaki, 2009a: Diurnal variation of precipitation over southeastern China: Spatial distribution and its seasonality. *J. Geophys. Res.*, **114**, D13103, https://doi.org/10.1029/2008JD011103.

——, ——, and ——, 2009b: Diurnal variation of precipitation over southeastern China: 2. Impact of the diurnal monsoon variability. *J. Geophys. Res.*, **114**, D21105, https://doi.org/10.1029/2009JD012181.

——, ——, M. Sawada, and T. Iwasaki, 2013: Influence of summer monsoon diurnal cycle on moisture transport and precipitation over eastern China. *J. Geophys. Res.*, **118**, 3163–3177, https://doi.org/10.1002/jgrd.50337.

——, T. Iwasaki, H. Qin, and W. Sha, 2014: Evaluation of the warm-season diurnal variability over East Asia in recent reanalyses JRA-55, ERA-Interim, NCEP CFSR, and NASA MERRA. *J. Climate*, **27**, 5517–5537, https://doi.org/10.1175/JCLI-D-14-00005.1.

——, W. Sha, T. Iwasaki, and Z. Wen, 2017: Diurnal cycle of a heavy rainfall corridor over East Asia. *Mon. Wea. Rev.*, **145**, 3365–3389, https://doi.org/10.1175/MWR-D-16-0423.1.

——, R. Lan, W. Zeng, H. Pan, and W. Li, 2018: Diurnal variations of rainfall in surface and satellite observations at the monsoon coast (South China). *J. Climate*, **31**, 1703–1724, https://doi.org/10.1175/JCLI-D-17-0373.1.

Chen, H., R. Yu, and Y. Shen, 2016: A new method to compare hourly rainfall between station observations and satellite products over central-eastern China. *J. Meteor. Res.*, **30**, 737–757, https://doi.org/10.1007/s13351-016-6002-5.

Chen, X., F. Zhang, and J. H. Ruppert, 2019: Modulations of the diurnal cycle of coastal rainfall over South China caused by the boreal summer intraseasonal oscillation. *J. Climate*, **32**, 2089–2108, https://doi.org/10.1175/JCLI-D-18-0786.1.

Ding, Y., 1992: Summer monsoon rainfalls in China. *J. Meteor. Soc. Japan*, **70**, 373–396, https://doi.org/10.2151/jmsj1965.70.1B_373.

——, and J. C. L. Chan, 2005: The East Asian summer monsoon: An overview. *Meteor. Atmos. Phys.*, **89**, 117–142, https://doi.org/10.1007/s00703-005-0125-z.

——, and Z. Wang, 2008: A study of rainy season in China. *Meteor. Atmos. Phys.*, **100**, 121–138, https://doi.org/10.1007/s00703-008-0299-2.

Dirmeyer, P. A., and Coauthors, 2012: Simulating the diurnal cycle of rainfall in global climate models: Resolution versus parameterization. *Climate Dyn.*, **39**, 399–418, https://doi.org/10.1007/s00382-011-1127-9.

Du, Y., and R. Rotunno, 2014: A simple analytical model of the nocturnal low-level jet over the Great Plains of the United States. *J. Atmos. Sci.*, **71**, 3674–3683, https://doi.org/10.1175/JAS-D-14-0060.1.

——, Q. Zhang, Y. Chen, Y. Zhao, and X. Wang, 2014: Numerical simulations of spatial distributions and diurnal variations of low-level jets in China during early summer. *J. Climate*, **27**, 5747–5767, https://doi.org/10.1175/JCLI-D-13-00571.1.

Fedorovich, E., J. A. Gibbs, and A. Shapiro, 2017: Numerical study of nocturnal low-level jets over gently sloping terrain. *J. Atmos. Sci.*, **74**, 2813–2834, https://doi.org/10.1175/JAS-D-17-0013.1.

Geng, B., and H. Yamada, 2007: Diurnal variations of the meiyu/baiu rain belt. *SOLA*, **3**, 61–64, https://doi.org/10.2151/sola.2007-016.

He, X., and Coauthors, 2015: The diurnal cycle of precipitation in regional spectral model simulations over West Africa: Sensitivities to resolution and cumulus schemes. *Wea. Forecasting*, **30**, 424–445, https://doi.org/10.1175/WAF-D-14-00013.1.

He, M., H. Liu, B. Wang, and D. Zhang, 2016: A modeling study of a low-level jet along the Yun-Gui Plateau in South China. *J. Appl. Meteor. Climatol.*, **55**, 41–60, https://doi.org/10.1175/JAMC-D-15-0067.1.

Holton, J. R., 1967: The diurnal boundary layer wind oscillation above sloping terrain. *Tellus*, **19A**, 200–205, https://doi.org/10.3402/tellusa.v19i2.9766.

Hu, X.-M., P. M. Klein, and M. Xue, 2013: Evaluation of the updated YSU planetary boundary layer scheme within WRF for wind resource and air quality assessments. *J. Geophys. Res. Atmos.*, **118**, 10 490–10 505, https://doi.org/10.1002/jgrd.50823.

Huang, W.-R., and Y.-H. Chang, 2018: Characteristics and mechanisms of the diurnal variation of winter precipitation in Taiwan. *Int. J. Climatol.*, **38**, 3058–3068, https://doi.org/10.1002/joc.5482.

Janowiak, J. E., V. E. Kousky, and R. J. Joyce, 2005: Diurnal cycle of precipitation determined from the CMORPH high spatial and temporal resolution global precipitation analyses. *J. Geophys. Res.*, **110**, D23105, https://doi.org/10.1029/2005JD006156.

Johnson, A., X. Wang, K. R. Haghi, and D. B. Parsons, 2018: Evaluation of forecasts of a convectively generated bore using an intensively observed case study from PECAN. *Mon. Wea. Rev.*, **146**, 3097–3122, https://doi.org/10.1175/MWR-D-18-0059.1.

Johnson, R., 2006: Mesoscale processes. *The Asian Monsoon*, B. Wang, Ed., Springer & Praxis Press, 331–356.

Joyce, R. J., J. E. Janowiak, P. A. Arkin, and P. Xie, 2004: CMORPH: A method that produces global precipitation estimates from passive microwave and infrared data at high spatial and temporal resolution. *J. Hydrometeor.*, **5**, 487–503, https://doi.org/10.1175/1525-7541(2004)005<0487:CAMTPG>2.0.CO;2.

Kobayashi, S., and Coauthors, 2015: The JRA-55 Reanalysis: General specifications and basic characteristics. *J. Meteor. Soc. Japan*, **93**, 5–48, https://doi.org/10.2151/jmsj.2015-001.

Li, J., and R. Yu, 2014: Characteristics of cold season rainfall over the Yungui Plateau. *J. Appl. Meteor. Climatol.*, **53**, 1750–1759, https://doi.org/10.1175/JAMC-D-13-0285.1.

——, S. Sorooshian, W. Higgins, X. Gao, B. Imam, and K. Hsu, 2008a: Influence of spatial resolution on diurnal variability during the North American monsoon. *J. Climate*, **21**, 3967–3988, https://doi.org/10.1175/2008JCLI2022.1.

——, R. Yu, and T. Zhou, 2008b: Seasonal variation of the diurnal cycle of rainfall in southern contiguous China. *J. Climate*, **21**, 6036–6043, https://doi.org/10.1175/2008JCLI2188.1.

Li, J. P., and J. Tang, 2012: Experiment of WRF multi-physics short-range ensemble forecasts in southeastern China (in Chinese). *J. Nanjing Univ.*, **48**, 677–688.

Li, P., F. Kalli, T. Zhou, H. Chen, J. Li, Z. Guo, and X. Chen, 2018: The diurnal cycle of East Asian summer monsoon precipitation simulated by the Met Office Unified Model at convection-permitting scales. *Climate Dyn.*, in press, https://doi.org/10.1007/s00382-018-4368-z.

Liu, H., L. Li, and B. Wang, 2012: Low-level jets over southeast China: The warm season climatology of the summer of 2003. *Atmos. Oceanic Sci. Lett.*, **5**, 394–400, https://doi.org/10.1080/16742834.2012.11447017.

Luo, Y., W. Qian, R. Zhang, and D.-L. Zang, 2013: Gridded hourly precipitation analysis from high-density rain gauge network

over the Yangtze–Huai Rivers Basin during the 2007 mei-yu season and comparison with CMORPH. *J. Hydrometeor.*, **14**, 1243–1258, https://doi.org/10.1175/JHM-D-12-0133.1.

Monaghan, A. J., D. L. Rife, J. O. Pinto, C. A. Davis, and J. R. Hannan, 2010: Global precipitation extremes associated with diurnally varying low-level jets. *J. Climate*, **23**, 5065–5084, https://doi.org/10.1175/2010JCLI3515.1.

Ninomiya, K., 2000: Large- and meso-α-scale characteristics of Meiyu/Baiu front associated with intense rainfalls in 1–10 July 1991. *J. Meteor. Soc. Japan*, **78**, 141–157, https://doi.org/10.2151/jmsj1965.78.2_141.

Ohsawa, T., H. Ueda, T. Hayashi, A. Watanabe, and J. Matsumoto, 2001: Diurnal variations of convective activity and rainfall in tropical Asia. *J. Meteor. Soc. Japan*, **79**, 333–352, https://doi.org/10.2151/jmsj.79.333.

Parish, T. R., and L. D. Oolman, 2010: On the role of sloping terrain in the forcing of the Great Plains low-level jet. *J. Atmos. Sci.*, **67**, 2690–2699, https://doi.org/10.1175/2010JAS3368.1.

Rao, X., K. Zhao, X. Chen, A. Huang, M. Xue, Q. Zhang, and M. Wang, 2019: Influence of synoptic pattern and low-level wind speed on intensity and diurnal variations of orographic convection in summer over Pearl River Delta, South China. *J. Geophys. Res.*, **124**, 6157–6179, https://doi.org/10.1029/2019JD030384.

Rife, D. L., J. O. Pinto, A. J. Monaghan, C. A. Davis, and J. R. Hannan, 2010: Global distribution and characteristics of diurnally varying low-level jets. *J. Climate*, **23**, 5041–5064, https://doi.org/10.1175/2010JCLI3514.1.

Satoh, M., and Y. Kitao, 2013: Numerical examination of the diurnal variation of summer precipitation over southern China. *SOLA*, **9**, 129–133, https://doi.org/10.2151/sola.2013-029.

Shapiro, A., E. Fedorovich, and S. Rahimi, 2016: A unified theory for the Great Plains nocturnal low-level jet. *J. Atmos. Sci.*, **73**, 3037–3057, https://doi.org/10.1175/JAS-D-15-0307.1.

Shen, Y., A. Xiong, Y. Wang, and P. Xie, 2010: Performance of high-resolution satellite precipitation products over China. *J. Geophys. Res.*, **115**, D02114, https://doi.org/10.1029/2010JD014481.

Shin, U., T.-Y. Lee, and S.-H. Park, 2019: Environment and processes for heavy rainfall in the early morning over the Korean penisula during episodes of cloud clusters associated with mesoscale troughs. *J. Meteor. Soc. Japan*, **97**, 633–655, https://doi.org/10.2151/jmsj.2019-036.

Shinoda, T., H. Uyeda, and K. Yoshimura, 2005: Structure of moist layer and sources of water over the southern region far from the Meiyu/Baiu Front. *J. Meteor. Soc. Japan*, **83**, 137–152, https://doi.org/10.2151/jmsj.83.137.

Skamarock, W. C., and J. B. Klemp, 2008: A time-split non-hydrostatic atmospheric model for weather research and forecasting applications. *J. Comput. Phys.*, **227**, 3465–3485, https://doi.org/10.1016/j.jcp.2007.01.037.

Sun, J., and F. Zhang, 2012: Impacts of mountain-plains solenoid on diurnal variations of rainfalls along the mei-yu front over the East China plains. *Mon. Wea. Rev.*, **140**, 379–397, https://doi.org/10.1175/MWR-D-11-00041.1.

Trier, S. B., C. A. Davis, D. A. Ahijevych, M. L. Weisman, and G. H. Bryan, 2006: Mechanisms supporting long-lived episodes of propagating nocturnal convection within a 7-day WRF model simulation. *J. Atmos. Sci.*, **63**, 2437–2461, https://doi.org/10.1175/JAS3768.1.

——, ——, and R. E. Carbone, 2014: Mechanisms governing the persistence and diurnal cycle of a heavy rainfall corridor. *J. Atmos. Sci.*, **71**, 4102–4126, https://doi.org/10.1175/JAS-D-14-0134.1.

——, J. W. Wilson, D. A. Ahijevych, and R. A. Sobash, 2017: Mesoscale vertical motions near nocturnal convection initiation in PECAN. *Mon. Wea. Rev.*, **145**, 2919–2941, https://doi.org/10.1175/MWR-D-17-0005.1.

Tuttle, J. D., and C. A. Davis, 2006: Corridors of warm season precipitation in the central United States. *Mon. Wea. Rev.*, **134**, 2297–2317, https://doi.org/10.1175/MWR3188.1.

Van de Wiel, B. J., A. F. Moene, G. J. Steeneveld, P. Baas, F. C. Bosveld, and A. A. Holtslag, 2010: A conceptual view on inertial oscillations and nocturnal low-level Jets. *J. Atmos. Sci.*, **67**, 2679–2689, https://doi.org/10.1175/2010JAS3289.1.

Wang, C.-C., G. T.-J. Chen, and R. E. Carbone, 2004: A climatology of warm-season cloud patterns over East Asia based on GMS infrared brightness temperature observations. *Mon. Wea. Rev.*, **132**, 1606–1629, https://doi.org/10.1175/1520-0493(2004)132<1606:ACOWCP>2.0.CO;2.

——, ——, H.-L. Huang, R. E. Carbone, and S.-W. Chang, 2012: Synoptic conditions associated with propagating and non-propagating cloud/rainfall episodes during the warm season over the East Asian continent. *Mon. Wea. Rev.*, **140**, 721–747, https://doi.org/10.1175/MWR-D-11-00067.1.

——, J. C.-S. Hsu, G. T.-J. Chen, and D.-I. Lee, 2014: A Study of two propagating heavy-rainfall episodes near Taiwan during SoWMEX/TiMREX IOP-8 in June 2008. Part II: Sensitivity tests on the roles of synoptic conditions and topographic effects. *Mon. Wea. Rev.*, **142**, 2644–2664, https://doi.org/10.1175/MWR-D-13-00330.1.

Wu, Y., A. Huang, D. Huang, F. Chen, B. Yang, Y. Zhou, D. Fang, L. Zhang, and L. Wen, 2018: Diurnal variations of summer precipitation over the regions east to Tibetan Plateau. *Climate Dyn.*, **51**, 4287–4307, https://doi.org/10.1007/s00382-017-4042-x.

Xue, M., X. Luo, K. Zhu, Z. Sun, and J. Fei, 2018: The controlling role of boundary layer inertial oscillations in Meiyu frontal precipitation and its diurnal cycles over China. *J. Geophys. Res. Atmos.*, **123**, 5090–5115, https://doi.org/10.1029/2018JD028368.

Yamada, H., B. Geng, H. Uyeda, and K. Tsuboki, 2007: Thermodynamic impact of the heated landmass on the nocturnal evolution of a cloud cluster over a Meiyu-Baiu front. *J. Meteor. Soc. Japan*, **85**, 663–685, https://doi.org/10.2151/jmsj.85.663.

Yang, S., and E. A. Smith, 2006: Mechanisms for diurnal variability of global tropical rainfall observed from TRMM. *J. Climate*, **19**, 5190–5226, https://doi.org/10.1175/JCLI3883.1.

Yin, S., D. Chen, and Y. Xie, 2009: Diurnal variations of precipitation during the warm season over China. *Int. J. Climatol.*, **29**, 1154–1170, https://doi.org/10.1002/joc.1758.

Yu, R., B. Wang, and T. Zhou, 2004: Climate effects of the deep continental stratus clouds generated by the Tibetan Plateau. *J. Climate*, **17**, 2702–2713, https://doi.org/10.1175/1520-0442(2004)017<2702:CEOTDC>2.0.CO;2.

——, T. Zhou, A. Xiong, Y. Zhu, and J. Li, 2007: Diurnal variations of summer precipitation over contiguous China. *Geophys. Res. Lett.*, **34**, L01704, https://doi.org/10.1029/2006GL028129.

——, J. Li, and H. Chen, 2009: Diurnal variation of surface wind over central eastern China. *Climate Dyn.*, **33**, 1089–1097, https://doi.org/10.1007/s00382-008-0478-3.

——, ——, ——, and W. Yuan, 2014: Progress in studies of the precipitation diurnal variation over contiguous China. *J. Meteor. Res.*, **28**, 877–902, https://doi.org/10.1007/s13351-014-3272-7.

Yuan, W., R. Yu, H. Chen, J. Li, and M. Zhang, 2010: Subseasonal characteristics of diurnal variation in summer monsoon

rainfall over central eastern China. *J. Climate*, **23**, 6684–6695, https://doi.org/10.1175/2010JCLI3805.1.

——, ——, M. Zhang, W. Lin, H. Chen, and J. Li, 2012: Regimes of diurnal variation of summer rainfall over subtropical East Asia. *J. Climate*, **25**, 3307–3320, https://doi.org/10.1175/JCLI-D-11-00288.1.

——, ——, and J. Li, 2013: Changes in the diurnal cycles of precipitation over eastern China in the past 40 years. *Adv. Atmos. Sci.*, **30**, 461–467, https://doi.org/10.1007/s00376-012-2092-x.

Zhang, Y., H. Chen, and R. Yu, 2014: Vertical structures and physical properties of the cold-season stratus clouds downstream of the Tibetan Plateau: Differences between daytime and nighttime. *J. Climate*, **27**, 6857–6876, https://doi.org/10.1175/JCLI-D-14-00063.1.

——, F. Zhang, C. A. Davis, and J. Sun, 2018: Diurnal evolution and structure of long-lived mesoscale convective vortices along the mei-yu front over the East China Plains. *J. Atmos. Sci.*, **75**, 1005–1025, https://doi.org/10.1175/JAS-D-17-0197.1.

——, M. Xue, K. Zhu, and B. Zhou, 2019: What is the main cause of diurnal variation and nocturnal peak of summer precipitation in Sichuan Basin, China? The key role of boundary layer low-level jet inertial oscillations. *J. Geophys. Res. Atmos.*, **124**, 2643–2664, https://doi.org/10.1029/2018JD029834.

Zheng, Y., K. Alapaty, J. A. Herwehe, A. D. Del Genio, and D. Niyogi, 2016: Improving high-resolution weather forecasts using the Weather Research and Forecasting (WRF) Model with an updated Kain–Fritsch scheme. *Mon. Wea. Rev.*, **144**, 833–860, https://doi.org/10.1175/MWR-D-15-0005.1.

Zhu, K., M. Xue, B. Zhou, K. Zhao, and Z. Sun, 2018: Evaluation of real-time convection-permitting precipitation forecasts in China during the 2013–2014 summer season. *J. Geophys. Res. Atmos.*, **123**, 1037–1064, https://doi.org/10.1002/2017JD027445.